1  # Energy-conservation datasets of global land surface radiation

2  # and heat fluxes from 2000-2020 generated by CoSEB

3  Junrui Wang[a, b], Ronglin Tang[a, b, *], Meng Liu[c], Zhao-Liang Li[a, b, c]

4  [a] State Key Laboratory of Resources and Environment Information System, Institute of

5  Geographic Sciences and Natural Resources Research, Chinese Academy of Sciences,

6  Beijing 100101, China

7  [b] University of Chinese Academy of Sciences, Beijing 100049, China

8  [c] State Key Laboratory of Efficient Utilization of Arable Land in China, Institute of

9  Agricultural Resources and Regional Planning, Chinese Academy of Agricultural

10  Sciences, Beijing 100081, China

11  * Authors to whom correspondence should be addressed: tangrl@lreis.ac.cn

12  **Abstract**

13  Accurately estimating global land surface radiation [including downward

14  shortwave radiation ($SW_{IN}$), downward longwave radiation ($LW_{IN}$), upward shortwave

15  radiation ($SW_{OUT}$), upward longwave radiation ($LW_{OUT}$) and net radiation (Rn)] and heat

16  fluxes [including latent heat flux (LE), soil heat flux (G) and sensible heat flux (H)] is

17  essential for quantifying the exchange of radiation, heat and water between the land and

18  atmosphere under global climate change. This study presents the first data-driven

19  energy-conservation datasets of global land surface radiation and heat fluxes from 2000

20  to 2020, generated by our model of Coordinated estimates of land Surface Energy

21  Balance components (CoSEB). The model integrates GLASS and MODIS remote

22  sensing data, ERA5-Land reanalysis datasets, topographic data, $CO_2$ concentration data

23  as independent variables and in situ radiation and heat flux observations at 258 eddy

24  covariance sites worldwide as dependent variables within a multivariate random forest

25  technique to effectively learn the physics of energy conservation. The developed

26  CoSEB-based datasets are strikingly advantageous in that [1] they are the first data-

27  driven global datasets that satisfy both surface radiation balance and heat balance

among the eight fluxes, as demonstrated by both the radiation imbalance ratio [RIR,

defined as $100\% \times (SW_{IN} - SW_{OUT} + LW_{IN} - LW_{OUT})/\text{Rn}$] and energy imbalance ratio

[EIR, defined as $100\% \times (\text{Rn} - \text{G} - \text{LE} - \text{H})/\text{Rn}$] of 0, [2] the radiation and heat fluxes

are characterized by high accuracies, where (1) the RMSEs ($R^2$) for daily estimates of

$SW_{IN}$, $SW_{OUT}$, $LW_{IN}$, $LW_{OUT}$, Rn, LE, H and G from the CoSEB-based datasets at 44

independent test sites were 37.52 W/m$^2$ (0.81), 14.20 W/m$^2$ (0.42), 22.47 W/m$^2$ (0.90),

13.78 W/m$^2$ (0.95), 29.66 W/m$^2$ (0.77), 30.87 W/m$^2$ (0.60), 29.75 W/m$^2$ (0.44) and 5.69

W/m$^2$ (0.44), respectively, (2) the CoSEB-based datasets, in comparison to the

mainstream products/datasets (i.e. GLASS, BESS-Rad, BESSV2.0, FLUXCOM,

MOD16A2, PML_V2 and ETMonitor) that generally separately estimated subsets of

the eight flux components, better agreed with the in situ observations. Our developed

datasets hold significant potential for application across diverse fields such as

agriculture, forestry, hydrology, meteorology, ecology, and environmental science,

which can facilitate comprehensive studies on the variability, impacts, responses,

adaptation strategies, and mitigation measures of global and regional land surface

radiation and heat fluxes under the influences of climate change and human activities.

The CoSEB-based datasets are open access and available through the National Tibetan

Plateau Data Center (TPDC) at https://doi.org/10.11888/Terre.tpdc.302559 (Tang et al.,

2025a) and through the Science Data Bank (ScienceDB) at

https://doi.org/10.57760/sciencedb.27228 (Tang et al., 2025b).

**Key words:** Surface energy balance; Surface radiation balance; Shortwave/Longwave

radiation; Net radiation; Sensible/Latent heat flux; Evapotranspiration; CoSEB


# 1 Introduction

Land surface radiation balance and heat balance play important roles in Earth's

climate system, representing the physical processes by which the surface-atmosphere

absorbs and redistributes radiation and heat fluxes (Berbery et al., 1999; Betts et al.,

1996; Mueller et al., 2009; Sellers et al., 1997; Xu et al., 2022a), and facilitating the

exchange of water, energy, carbon, and other agents essential to climatic and ecological

56    systems and human society (Jia et al., 2013; Wang et al., 2012; Wild, 2009; Wild et al.,

57    2012; Xia et al., 2006). Accurately monitoring the spatial and temporal variations of

58    global land surface radiation [including downward shortwave radiation ($SW_{IN}$),

59    downward longwave radiation ($LW_{IN}$), upward shortwave radiation ($SW_{OUT}$), upward

60    longwave radiation ($LW_{OUT}$) and net radiation (Rn)] and heat fluxes [including latent

61    heat flux (LE), soil heat flux (G) and sensible heat flux (H)] is indispensable for

62    quantifying the exchange of radiation, heat and water between the land and atmosphere

63    under global climate change (Ersi et al., 2024; Liang et al., 2019; Rios & Ramamurthy,

64    2022; Tang et al., 2024a; Wang et al., 2021), and for studying solar energy utilization

65    (Tang et al., 2024b; Zhang et al., 2017), hydrological cycle (Huang et al., 2015; Wild &

66    Liepert, 2010), ecosystem productivity (Nemani et al., 2003), agricultural management

67    (De Wit et al., 2005) and ecological protection (Tang et al., 2023). Remote sensing (RS)

68    technology, with its high spatial-temporal resolution and applicability over large areas,

69    is considered to be the most effective and economical means for obtaining global land

70    surface radiation and heat fluxes (Liu et al., 2016; Van Der Tol, 2012; Zhang et al.,

71    2010).

72        In past decades, numerous RS-based products/datasets of global surface radiation

73    and heat fluxes have significantly advanced, which were generally generated by

74    physical (Li et al., 2023; Mu et al., 2011; Yu et al., 2022) or statistical methods (Jiao et

75    al., 2023; Jung et al., 2019; Peng et al., 2020). However, two key limitations still exist

76    in these products. Firstly, most available products provide only a single component of

77    land surface radiation or heat fluxes, e.g. ETMonitor (Zheng et al., 2022) and

78    MOD16A2 (Mu et al., 2011) only estimating LE, leading to the failure to satisfy surface

79    radiation balance and heat balance when the single radiation or heat flux is utilized in

80    conjunction with products containing other radiation and heat components (Wang et al.,

81    2025), and further posing significant uncertainties to understand the interactions and

82    redistributions of surface radiation and energy in the Earth-atmosphere system.

83    Secondly, a few products, e.g., FLUXCOM (Jung et al., 2019) and GLASS (Jiang et al.,

84  2015; Zhang et al., 2014), generated datasets for multiple components of surface

85  radiation and heat fluxes by using separate estimates from the uncoordinated models,

86  which make them difficult to abide by surface radiation and heat conservation. These

87  energy-imbalanced and radiation-imbalanced estimates among multiple components

88  from previous products/datasets severely limit their in-depth applications in analyzing

89  the spatial and temporal trends, simulating the physical processes of radiation, heat and

90  water cycles as well as revealing the attributions and mechanisms in Earth-surface

91  system under global climate change. It was imperative to develop global datasets of

92  land surface radiation and heat fluxes characterized by high accuracy, radiation balance

93  as well as heat balance, to better meet the requirements in practical applications of

94  various fields.

95      Our proposed data-driven model/framework of Coordinated estimates of land

96  Surface Energy Balance components (CoSEB) (Wang et al., 2025), which effectively

97  learns the underlying physical interrelations (i.e., surface energy conservation law)

98  among multiple targeted variables, provides an unprecedented opportunity to develop

99  global datasets of land surface radiation and heat fluxes that can not only

100  simultaneously provide high-accuracy estimates of these components but also adhere

101  to surface radiation- and heat-conservation laws.

102      The objectives of this study are twofold: (1) to develop high-accuracy datasets of

103  global land surface radiation and heat fluxes, which comply with the principles of

104  radiation balance and heat balance, using our CoSEB model renewed based on in situ

105  observations, remote sensing data and reanalysis datasets; (2) to validate the

106  datasets/model estimates against data from in situ observations, mainstream products

107  as well as estimates from uncoordinated random forest (RF) techniques. Section 2

108  introduces the data resources used in this study. Section 3 briefly describes the method

109  we used to estimate global surface radiation and heat fluxes. Section 4 presents the

110  evaluation of the datasets/model estimates generated by our renewed CoSEB model.

111  Section 5 discusses the superiority, potential applications and uncertainties of the

112 developed datasets. Data availability is given in Section 6, and a summary and
113 conclusion is provided in Section 7.

114 **2 Data**

115 **2.1 Ground-based observations**

116 In this study, the in situ observations of land surface radiation and heat fluxes at

117 302 eddy covariance (EC) sites from the networks of AmeriFlux (174 sites, 2000–2020,

118 https://AmeriFlux.lbl.gov/Data/, last access: 6 August 2024), EuroFlux (72 sites, 2000-

119 2020, http://www.europe-fluxdata.eu/, last access: 6 August 2024), OzFlux (5 sites,

120 2007-2012, https://data.ozflux.org.au/, last access: 6 August 2024), FLUXNET (108

121 sites, 2000–2014, https://FLUXNET.org/Data/download-Data/, last access: 6 August

122 2024), JapanFlux (15 sites, 2001-2020, https://ads.nipr.ac.jp/japan-flux2024/, last

123 access: 10 October 2025), ChinaFLUX (5 sites, 2005-2020, http://www.chinaflux.org/,

124 last access: 6 August 2024) and National Tibetan Plateau/Third Pole Environment Data

125 Center (TPDC, 13 sites, 2012–2020, https://Data.tpdc.ac.cn/en/Data, last access: 6

126 August 2024) were used (Fig. 1), where 37, 48 and 5 sites in FLUXNET were also

127 shared in AmeriFlux, EuroFlux and OzFlux, respectively. These 302 sites were filtered

128 out from all collected 1098 sites by following the quality-assurance and quality-control

129 steps, including: (1) any site with a missing component of any of the $SW_{IN}$, $SW_{OUT}$, $LW_{IN}$,

130 $LW_{OUT}$, LE, H and G was excluded, reducing the 1098 sites to 472 sites for further

131 analysis; (2) any half-hour period with missing data for any of these components was

132 excluded; (3) the half-hourly ground-based observations with quality-control flag of 2

133 or 3 (bad quality) were removed but quality-control flag of 0 and 1 (good quality) were

134 maintained; (4) a daily average of the half-hour observations was calculated for each

135 day with greater than 80% good-quality data, further reducing the 472 sites to 355 sites;

136 (5) the aggregated daily LE and H were corrected for energy imbalance using the

137 Bowen ratio method when the daily energy balance closure [defined as

138 $\left(LE+H\right)/\left(Rn-G\right)$ ] varied between 0.2 and 1.8 following Wang et al. (2025) to

139 exclude physically implausible measurements; (6) extreme outliers in the daily

140 evaporative fraction were further removed by excluding values outside the 1st–99th

141 percentile range, a common practice in flux and remote sensing studies (Bartkowiak et

142 al., 2024; Wang et al., 2023), further reducing the 355 sites to 337 sites. Besides, the RS

143 products/datasets involved in this study collocated at the sites should not be missing,

144 finally reducing the 337 sites to 302 sites for analysis. Note that the Rn at these sites

145 used in this study was calculated from the sum of net longwave radiation ($LW_{IN}$ minus

146 $LW_{OUT}$) and net shortwave radiation ($SW_{IN}$ minus $SW_{OUT}$), rather than using the

147 observed Rn directly, to ensure surface radiation balance in training datasets.

148      These 302 sites used in this study cover a wide range of global climate regimes

149 across 14 land cover types, including (1) evergreen needleleaf forests (ENF, 55 sites);

150 (2) evergreen broadleaf forests (EBF, 12 sites); (3) deciduous needleleaf forests (DNF,

151 7 sites); (4) deciduous broadleaf forests (DBF, 40 sites); (5) mixed forests (MF, 8 sites);

152 (6) closed shrublands (CSH, 5 sites); (7) open shrublands (OSH, 11 sites); (8) woody

153 savannas (WSA, 6 sites); (9) savannas (SAV, 10 sites); (10) grasslands (GRA, 62 sites);

154 (11) permanent wetlands (WET, 22 sites); (12) croplands (CRO, 59 sites); (13) water

155 bodies (WAT, 1 sites); (14) cropland/natural vegetation mosaics (CVM, 4 sites). Among

156 them, 44 sites (~15% of the total, see Table S1) were isolated to serve as spatially

157 independent sites to test the generated datasets and they did not participate in the

158 development of the model/datasets.

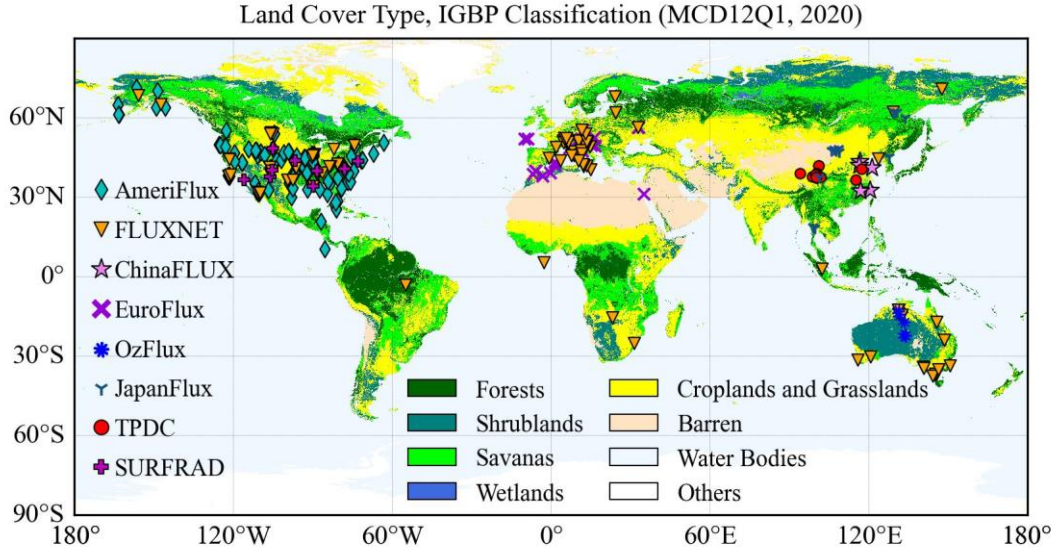**Land Cover Type, IGBP Classification (MCD12Q1, 2020)**

159

160 **Fig. 1 Spatial distribution of the 302 eddy covariance sites from AmeriFlux, FLUXNET,**
161 **EuroFlux, OzFlux, JapanFlux, ChinaFLUX and TPDC, and nine radiation sites from**
162 **SURFRAD involved for analysis in this study.**

163       Furthermore, ground-based radiation observations from nine sites that are located

164 in large flat agricultural areas covered by crops and grasses from SURFRAD

165 (https://gml.noaa.gov/) were also introduced to validate land surface radiation estimates.

166 Similar to the preprocessing performed on the observations of the 302 EC sites, the

167 $SW_{IN}$, $SW_{OUT}$, $LW_{IN}$, $LW_{OUT}$ and Rn from the SURFRAD were also quality-controlled

168 and aggregated to daily data. Spatial distribution of the 302 EC sites and nine radiation

169 sites from SURFRAD are shown in Fig. 1, with site details (latitude, longitude, land

170 cover types, digital elevation model and temporal coverage) provided in Supplementary

171 Tables S1 and S2.

172 **2.2 Climate/meteorology and remote sensing data**

173       To generate global datasets of land surface radiation and heat fluxes from 2000 to

174 2020, five types of climate/meteorology and remote sensing data were used in this study,

175 including:

176 (1)   ERA5-Land reanalysis datasets (https://cds.climate.copernicus.eu/, last access: 6

177       August 2024) with the spatial resolution of ~9 km from 1950 (Muñoz-Sabater et

178       al., 2021). Following our previous work (Wang et al., 2025), this study used

179      variables from the ERA5-Land datasets to drive the model, including near-surface

180      2 m air temperature ($T_a$), soil temperature in layer 1 (0-7 cm, $T_{S1}$), soil volumetric

181      moisture content in layer 1 (0-7 cm, $SM1$), solar radiation reaching the surface of

182      the earth ($SW_{IN}^{ERA5}$), net thermal radiation at the surface ($LW_{net}$), pressure of the

183      atmosphere ($PA$), 10 m wind speed ($WS$), precipitation ($P_r$) and the 2 m dewpoint

184      temperature, daily minimum and maximum air temperature [for calculating

185      relative air humidity ($RH$)].

186    (2)   GLASS datasets (https://glass.bnu.edu.cn/, last access: 6 August 2024), which

187         provide the 500 m 8-day leaf area index ($LAI$) and fractional vegetation cover

188         ($FVC$) from February 2000 to December 2021.

189    (3)   MOD44B product (https://lpdaac.usgs.gov/, last access: 6 August 2024), which

190         offers yearly 250 m percent tree cover ($PTC$) since 2000, representing the

191         percentage (0~100%) of a pixel covered by tree canopy.

192    (4)   NOAA/GML atmospheric carbon dioxide ($CO_2$) concentration data, providing

193         monthly global marine surface mean data since 1958

194         (ftp://aftp.cmdl.noaa.gov/products/trends/co2/co2_mm_gl.txt, last access: 6

195         August 2024).

196    (5)   GMTED2010 topographic data

197         (https://topotools.cr.usgs.gov/gmted_viewer/gmted2010_global_grids.php, last

198         access: 6 August 2024), providing 500 m digital elevation model (DEM), slope,

199         and aspect.

200      The ~9 km ERA5-Land datasets were spatially interpolated to 500 m using the

201 cubic convolution method, and the 250 m PTC was resampled to 500 m using the

202 arithmetic averaging method.

203 **2.3 Mainstream datasets/products for inter-comparison**

204      Mainstream RS-based datasets/products of moderate-resolution global land

205 surface radiation and heat fluxes were collected for inter-comparison (Table 1),

206 including (1) the daily 0.05° GLASS $SW_{IN}$, $LW_{IN}$, $LW_{OUT}$ and Rn products from 2000 to

207 2018 (https://glass.bnu.edu.cn/, last access: 6 August 2024), (2) the daily 0.05°

208 Breathing Earth System Simulator Radiation (BESS-Rad) $SW_{IN}$ products from 2000 to

209 2020 (https://www.environment.snu.ac.kr/bess-rad), (3) the daily 0.05° BESS

210 Version2.0 (BESSV2.0) Rn and LE products from 2000 to 2020

211 (https://www.environment.snu.ac.kr/bessv2), (4) the 8-day 0.0833° FLUXCOM Rn, LE

212 and H products from 2001 to 2020 (https://fluxcom.org/, last access: 6 August 2024),

213 (5) the daily 1 km ETMonitor LE product from 2000 to 2020 (https://data.casearth.cn/,

214 last access: 6 August 2024), (6) the 8-day 500 m Penman-Monteith-Leuning Version2

215 (PML_V2, https://www.tpdc.ac.cn/, last access: 6 August 2024) LE product from 2000

216 to 2020; and (7) the 8-day 500 m MOD16A2 (https://lpdaac.usgs.gov/, last access: 6

217 August 2024) LE product from 2000 to 2020.

218      The GLASS $SW_{IN}$ products are derived from a combination of the GLASS

219 broadband albedo product and the surface shortwave net radiation estimates, where the

220 surface shortwave net radiation is estimated using linear regression with MODIS top-

221 of-atmosphere (TOA) spectral reflectance (Wang et al., 2015). The GLASS $LW_{IN}$ and

222 $LW_{OUT}$ products are generated using densely connected convolutional neural networks,

223 incorporating Advanced Very High-Resolution Radiometer (AVHRR) TOA reflectance

224 and ERA5 near-surface meteorological data (Xu et al., 2022b). The GLASS Rn

225 products are estimated from the meteorological variables from MERRA2 and surface

226 variables from GLASS using the multivariate adaptive regression splines model (Jiang

227 et al., 2015). The BESS-Rad and BESSV2.0 estimate $SW_{IN}$ and Rn using a radiative

228 transfer model (i.e., Forest Light Environmental Simulator, FLiES) with an artificial

229 neural network based on MODIS and MERRA2 reanalysis datasets, and using FLiES

230 based on MODIS products and NCEP/NCAR reanalysis data, respectively (Li et al.,

231 2023; Ryu et al., 2018). Moreover, the BESSV2.0 (Li et al., 2023), MOD16A2 (Mu et

232 al., 2011), PML_V2 (Zhang et al., 2019) and ETMonitor (Zheng et al., 2022) generated

233 global LE by physical models, such as Penman-Monteith equation, Priestley-Taylor

234    equation and/or Shuttleworth-Wallace two-source scheme. The FLUXCOM Rn, LE and

235    H datasets are obtained through multiple machine learning methods based on in situ

236    observations from FLUXNET and remote sensing and meteorological data (Jung et al.,

237    2019). For better consistency, RF-based 8-day 0.0833° Rn and Bowen ratio-corrected

238    LE and H for the periods of 2000 to 2020 from the FLUXCOM were used in this study.

239    **Table 1 Summary of mainstream datasets/products for inter-comparison used in this study**

| Products/ datasets | Reso- lution | Time coverage | Variables | Algorithms | References |
|---|---|---|---|---|---|
| GLASS | 0.05°/ daily | 2000-2018 | $SW_{IN}$, $LW_{IN}$, $LW_{OUT}$, Rn | Machine learning, direct estimation algorithm | Wang et al. (2015); Xu et al. (2022b); Jiang et al. (2015) |
| BESS-Rad | 0.05°/ daily | 2000-2020 | $SW_{IN}$ | BESS process model | Ryu et al. (2018) |
| BESSV2.0 | 0.05°/ daily | 2000-2020 | Rn, LE | BESS process model | Li et al. (2023) |
| FLUXCOM | 0.0833°/ 8-day | 2000-2020 | Rn, LE, H | Model tree ensembles | Jung et al. (2019) |
| MOD16A2 | 500 m/ 8-day | 2000-2020 | LE | Modified Penman-Monteith equation | Mu et al. (2011) |
| PML_V2 | 500 m/ 8-day | 2002-2020 | LE | Penman Monteith-Leuning model, Priestley Taylor equation and Gash model | Zhang et al. (2019) |
| ETMonitor | 1 km/ daily | 2000-2020 | LE | Shuttleworth-Wallace two-source scheme, Gash model and Penman equation | Zheng et al. (2022) |

## 3 Methods

241    The method used to generate global datasets of land surface radiation and heat

242    fluxes is based on the CoSEB model/framework, which was developed by our

243    previously published work (Wang et al., 2025), to coordinately estimate global land

244    surface energy balance components (including Rn, LE, H and G) using the multivariate

245    random forest technique, with a combination of MODIS and GLASS products, ERA5-

246    Land reanalysis datasets, and in situ observations at 336 EC sites. The CoSEB model

247    was demonstrated to be able to produce high-accuracy estimates of land surface energy

248    components, with the RMSE of <17 W/m$^2$ and R$^2$ of > 0.83 for estimating 4-day Rn,

249    LE and H, and the RMSE of <5 W/m$^2$ and R$^2$ of 0.55 for estimating 4-day G. The most

250    praiseworthy superiority of the CoSEB model lies in its ability to balance the land

251    surface energy components, with an energy imbalance ratio [EIR, defined as 100%×

252    (Rn - G - LE - H)/Rn] of 0.

253        To coordinately estimate land surface radiation and heat fluxes that comply with

254    both radiation balance and heat balance, one of the key procedures in the construction

255    of the CoSEB model was to prepare training datasets that satisfy surface radiation and

256    heat balance. For this purpose, the energy-imbalance corrections on daily in situ

257    observed LE and H were conducted by the most widely applied Bowen ratio method

258    [ $H^{corr} = \dfrac{H}{H+LE} \times (Rn-G)$, $LE^{corr} = \dfrac{LE}{H+LE} \times (Rn-G)$, where $H^{corr}$ and $LE^{corr}$

259    represent the sensible heat flux and latent heat flux after energy-imbalance correction,

260    respectively] with the aid of Rn and G observations, and the in situ Rn was calculated

261    from the sum of in situ observed net longwave radiation ($LW_{IN}$ minus $LW_{OUT}$) and net

262    shortwave radiation ($SW_{IN}$ minus $SW_{OUT}$). The input variables to renew the CoSEB

263    model include: (1) climate/meteorology: $T_a$, $SW_{IN}^{ERA5}$, $LW_{net}$, $WS$, $PA$, $P_r$, $RH$,

264    $CO_2$ concentration; (2) vegetation and soil: *LAI*, *FVC*, *PTC*, $T_{S1}$, *SM1*; (3) topography

265    data: *DEM*, *Slope* and *Aspect*, in addition to longitude (*Lon*), latitude (*Lat*), and inverse

266    relative distance from the Earth to the Sun (*dr*), in which the *dr* was calculated as

267    $dr = 1 + 0.033 \times \cos\left(\dfrac{2\pi \times DOY}{365}\right)$, where *DOY* represents the day of year. Considering

268    that the footprint of the site-based measurements of turbulent heat fluxes is generally at

269    a scale of hundreds of meters, to reduce the effect of differences of spatial scales

270    between ground-based measurements (dependent variables) and remotely

271    sensed/reanalysis datasets (independent variables), we renewed the CoSEB model at a

272    spatial scale of 500 m for coordinately estimating global daily land surface radiation

273    and heat fluxes, which can be expressed as follows:

274    $$\begin{pmatrix} SW_{IN}, SW_{OUT}, LW_{IN}, \\ LW_{OUT}, Rn, LE, H, G \end{pmatrix} = f \begin{pmatrix} Lon, Lat, T_a, T_{S1}, SM1, SW_{IN}^{ERA5}, LW_{net}, PA, WS, P_r, dr \\ RH, LAI, FVC, PTC, DEM, Slope, Aspect, CO_2 \end{pmatrix} (1)$$

275    To enhance model generalization, the renewed CoSEB model was reoptimized

276    using random and grid search methods, resulting in different hyperparameters of 281

277    decision trees, a maximum depth of 21, and minimum samples split and leaf of 8 from

278    those of Wang et al. (2025). Site-based 10-fold cross-validation was employed to

279    evaluate the transferability and generalization of the CoSEB model by randomly

280    dividing all sites into ten folds, where the samples from each fold of sites in turn served

281    as validation datasets while the remaining folds were used as training datasets, ensuring

282    that the validation was conducted on sites spatially independent from the training data.

283    Furthermore, to benchmark the coordinated estimates from the renewed CoSEB model,

284    eight RF-based uncoordinated models were constructed, each separately estimating one

285    of $SW_{IN}$, $SW_{OUT}$, $LW_{IN}$, $LW_{OUT}$, Rn, LE, H or G using the same inputs as those in the

286    renewed CoSEB model. Fig. 2 illustrates the flowchart for generating global datasets

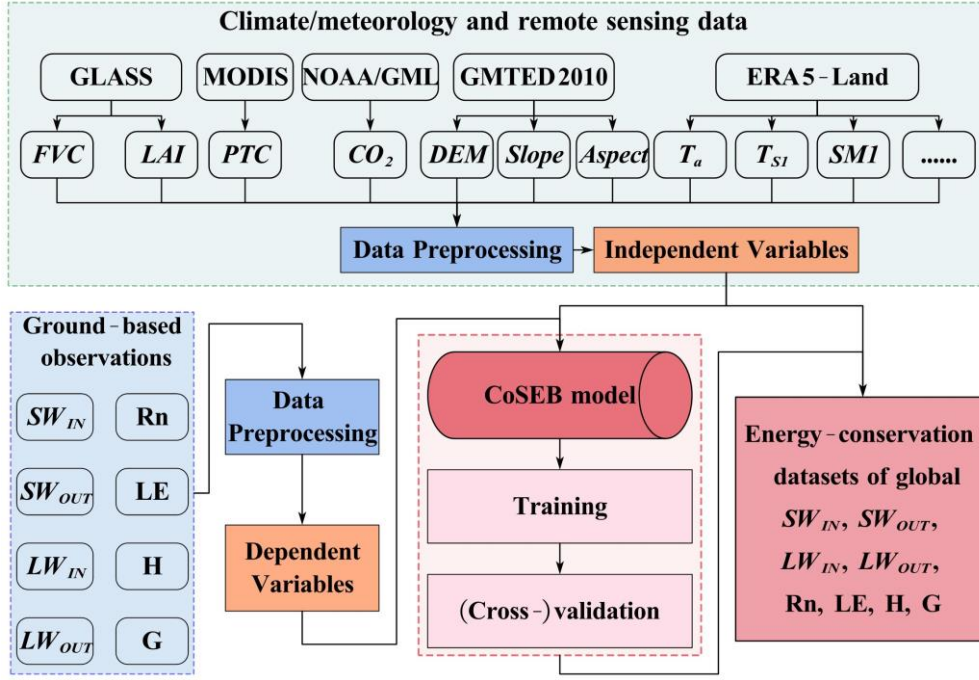287    of land surface radiation and heat fluxes by the CoSEB model.

288

**Fig. 2 Flowchart for generating energy-conservation datasets of global land surface radiation [including downward shortwave radiation ($SW_{IN}$), downward longwave radiation ($LW_{IN}$), upward shortwave radiation ($SW_{OUT}$), upward longwave radiation ($LW_{OUT}$) and net radiation (Rn)] and heat fluxes [including latent heat flux (LE), soil heat flux (G) and sensible heat flux (H)] by the CoSEB model renewed from in situ observations at 258 sites worldwide and collocated remote sensing and reanalysis datasets.**

## 4 Results

### 4.1 Validation of the CoSEB model

#### 4.1.1 Site-based 10-fold cross-validations at 258 EC sites

Fig. 3 and Fig. 4 present the scatter density plots of the site-based 10-fold cross-validation of daily $SW_{IN}$, $LW_{IN}$, $SW_{OUT}$, $LW_{OUT}$, Rn, LE, H and G estimated from the renewed CoSEB model and the RF-based uncoordinated models, respectively, by using the validation datasets collected at 258 EC sites worldwide. Results indicated that the estimates from both the CoSEB model and the RF-based uncoordinated models agreed well with the in situ observations, with the coefficient of determination ($R^2$) varying between 0.80 and 0.95 for $SW_{IN}$, $LW_{IN}$, $LW_{OUT}$ and Rn, and between 0.59 and 0.67 for $SW_{OUT}$, LE and H. The CoSEB model, with the root mean square error (RMSE) of 26.82 to 34.25 W/m$^2$ and mean absolute error (MAE) of 18.83 to 24.49 W/m$^2$ for $SW_{IN}$, Rn, LE and H, the RMSE of 12.24 to 17.75 W/m$^2$ and the MAE of 8.39 to 13.70 W/m$^2$ for

13

308      $SW_{OUT}$, $LW_{IN}$ and $LW_{OUT}$, demonstrated comparable accuracies to the RF-based models,

309      with the RMSE of 27.07 to 33.34 W/m$^2$ and MAE of 19.29 to 23.64 W/m$^2$ for $SW_{IN}$,

310      Rn, LE and H, the RMSE of 12.12 to 16.93 W/m$^2$ and the MAE of 8.68 to 12.99 W/m$^2$

311      for $SW_{OUT}$, $LW_{IN}$ and $LW_{OUT}$. In the validation of daily G, both the CoSEB and RF-based

312      models yielded RMSEs below 7 W/m$^2$. Comparisons with the corresponding training

313      results (Table S3 in the Supplementary Material) indicated that although the CoSEB

314      model performed better on the training datasets, its overall performance remained stable,

315      suggesting that the CoSEB model was not affected by overfitting.

316          Strikingly, the CoSEB model exhibited large superiority in balancing the surface

317      radiation and heat fluxes, with the radiation imbalance ratio [RIR, defined as 100% ×

318      ($SW_{IN} - SW_{OUT} + LW_{IN} - LW_{OUT}$)/Rn] and energy imbalance ratio [EIR, defined as 100%

319      × (Rn - G - LE - H)/Rn] of 0, while the RF-based uncoordinated models showed

320      substantial imbalances of the surface radiation and heat fluxes, with RIR and EIR that

321      were approximately normally distributed, having absolute mean values of 38.84% and

322      31.22%, respectively, and reaching as high as 50% in some cases. Furthermore, the RIR

323      as well as EIR tended to be higher under lower solar radiation, air temperature, or FVC,

324      with more frequent low values of these three variables leading to a broader and less

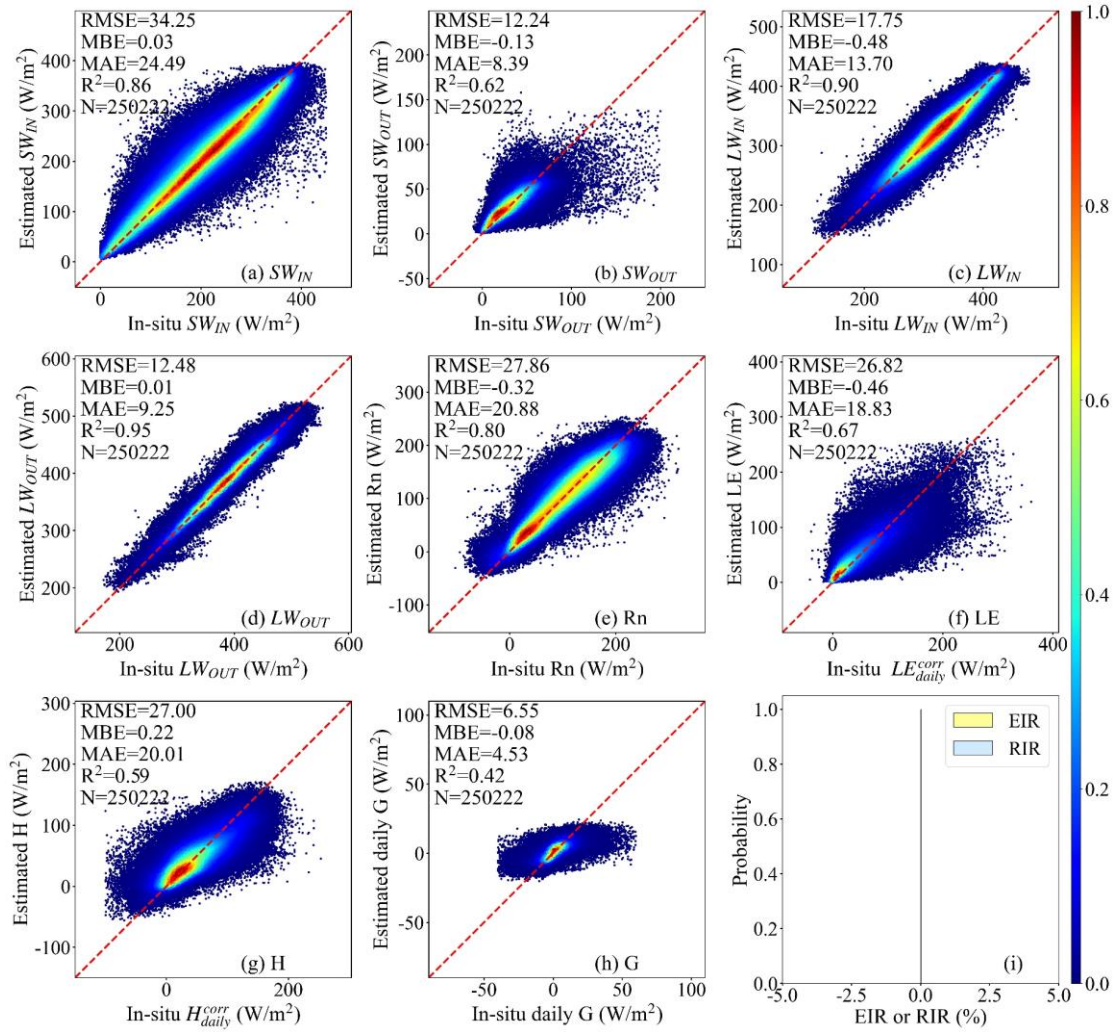325      peaked distribution of RIR and EIR (see Fig. S1 in the Supplementary Material).

Fig. 3 Scatter density plots of the site-based 10-fold cross-validation of daily downward shortwave and longwave radiation ($SW_{IN}$ and $LW_{IN}$), upward shortwave and longwave radiation ($SW_{OUT}$ and $LW_{OUT}$), net radiation (Rn), soil heat flux (G), latent heat flux (LE) and sensible heat flux (H) derived by the CoSEB model against in situ observed $SW_{IN}$, $LW_{IN}$, $SW_{OUT}$, $LW_{OUT}$, Rn, G, and energy imbalance-corrected LE ($LE_{daily}^{corr}$) and H ($H_{daily}^{corr}$). The EIR and RIR in the subfigure (i) represent the energy imbalance ratio and radiation imbalance ratio, which are defined as $100\% \times (Rn - G - LE - H)/Rn$ and $100\% \times (SW_{IN} - SW_{OUT} + LW_{IN} - LW_{OUT})/Rn$, respectively. The colorbar represents the normalized density of data points.

335
336 **Fig. 4 Same as Fig. 3, but for estimates from RF-based uncoordinated models.**

337 **4.1.2 Validation at nine radiation sites from SURFRAD**

338       To further illustrate the generality and transferability of the renewed CoSEB model,

339 the validation of estimates of the five radiation components (including $SW_{IN}$, $SW_{OUT}$,

340 $LW_{IN}$, $LW_{OUT}$, Rn) derived from both the CoSEB model and RF-based uncoordinated

341 models against observations at nine radiation sites from SURFRAD was performed, as

342 shown in Fig. 5. The results showed that both the CoSEB model and the RF-based

343 models achieved high accuracy in estimating daily $SW_{IN}$, $SW_{OUT}$, $LW_{IN}$, $LW_{OUT}$ and Rn,

344 with the RMSE of ~30 W/m$^2$ for $SW_{IN}$, ~14 W/m$^2$ for $SW_{OUT}$ and $LW_{IN}$, ~12 W/m$^2$ for

345 $LW_{OUT}$ and ~24 W/m$^2$ for Rn, with the R$^2$ >0.9 for $SW_{IN}$, $LW_{IN}$ and $LW_{OUT}$, ~0.65 for

346 $SW_{OUT}$ and ~0.85 for Rn. Compared to the results of the site-based 10-fold cross-

347 validation at 258 EC sites, the performances at nine radiation sites showed slight

16

348 improvements, with the RMSE decreasing by 0.74 to 4.54 $W/m^2$ for $SW_{IN}$, $LW_{IN}$, $LW_{OUT}$

349 and Rn in the CoSEB model, but a slight degradation with the RMSE increasing by

350 ~1.05 $W/m^2$ for $SW_{OUT}$, suggesting the robust performance of the CoSEB model.

351 Furthermore, the CoSEB model demonstrated a large superiority in maintaining surface

352 radiation balance among the five radiation components, with the RIR of 0, in contrast

353 to the RF-based models, which failed to meet this balance, exhibiting significant RIR

354 exceeding 50%.

355 **4.2 Validation and inter-comparisons of the CoSEB-based datasets**

356 As demonstrated in Section 4.1, the renewed CoSEB model with a spatial scale of

357 500 m achieved comparable accuracies to the RF-based uncoordinated models but

358 outperformed them in balancing surface radiation and heat fluxes. Evidenced by the

359 validation for its superiority, the renewed CoSEB model was then applied to the

360 spatially aggregated input datasets to generate our developed global daily datasets with

361 a spatial resolution of 0.05°. To further assess the performance of the developed

362 CoSEB-based datasets, in situ observations from another 44 spatially independent test

363 sites (see Section 2.1), which were not involved in model construction and datasets

364 generation, were used for validation. Mainstream products (i.e. GLASS, BESS-Rad,

365 BESSV2.0, FLUXCOM, PML_V2, MOD16A2 and ETMonitor) were also involved for

366 inter-comparison at the 44 test sites.

367 Note that due to the lack of moderate-resolution global RS-based products/datasets

368 of daily and/or 8-day $SW_{OUT}$, H and G, the intercomparison between different

369 products/datasets was impossible. Instead, we conducted a validation of these

370 components from the CoSEB-based datasets against in situ observations at 44 test sites,

371 as shown in Figs S2 and S3 in the Supplementary Material. Results indicated that the

372 CoSEB-based datasets could provide good estimates of $SW_{OUT}$, H and G, with the

373 RMSEs ($R^2$) of 14.20 $W/m^2$ (0.42), 29.75 $W/m^2$ (0.44) and 5.69 $W/m^2$ (0.44) at daily

374 scale, respectively, and the RMSE ($R^2$) of 12.19 $W/m^2$ (0.39) and 4.60 $W/m^2$ (0.47) for
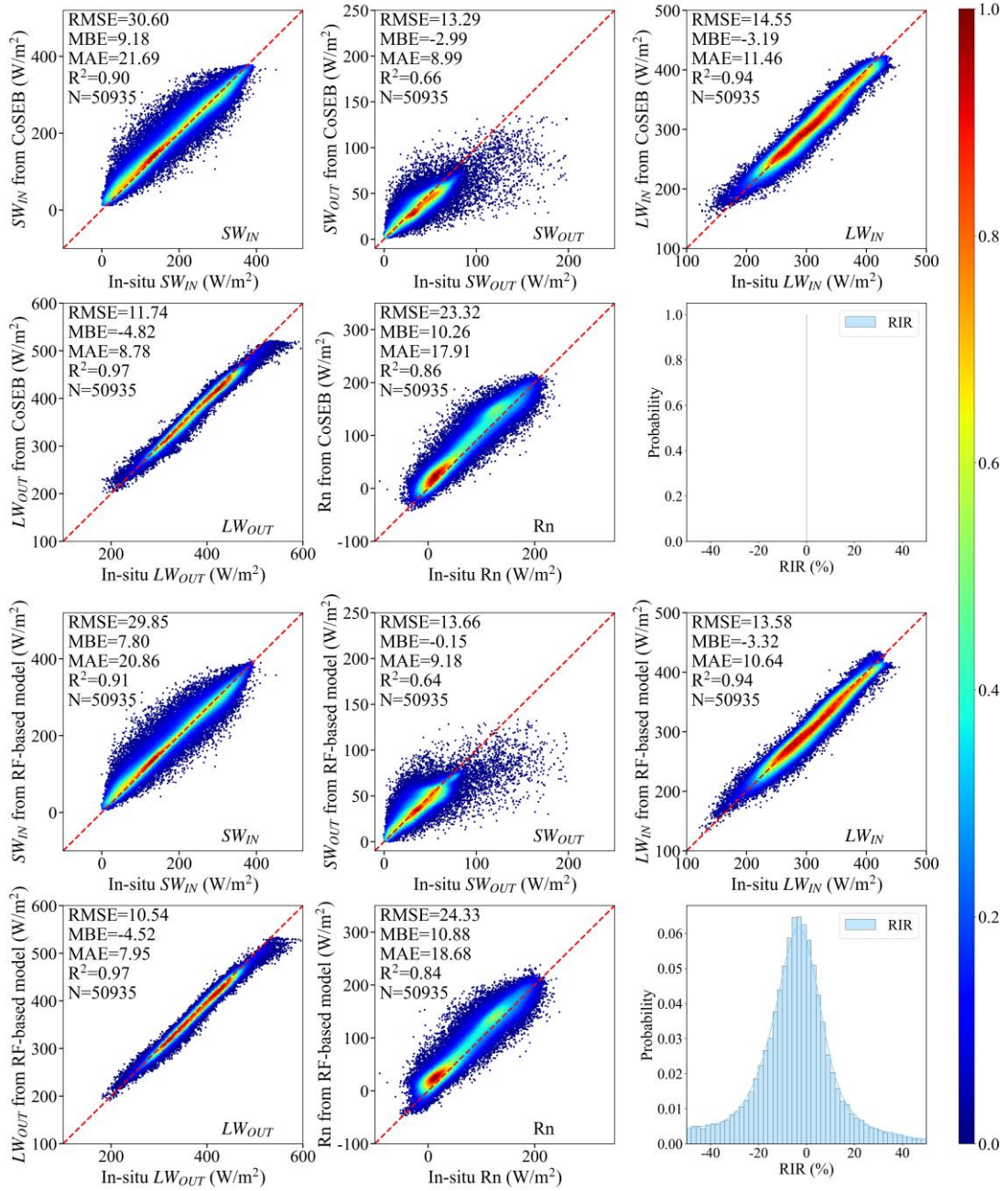
375 8-day $SW_{OUT}$ and G, respectively.

**Fig. 5 Scatter density plots of the validation of daily downward shortwave and longwave radiation ($SW_{IN}$ and $LW_{IN}$), upward shortwave and longwave radiation ($SW_{OUT}$ and $LW_{OUT}$) and net radiation (Rn) from the renewed CoSEB model (upper two rows) and RF-based uncoordinated models (lower two rows) against in situ observations at nine radiation sites from SURFRAD. The RIR represents the radiation imbalance ratio, defined as 100% × ($SW_{IN}$ − $SW_{OUT}$ + $LW_{IN}$ - $LW_{OUT}$)/Rn. The colorbar represents the normalized density of data points.**

Fig. 6 and Fig. 7 present the comparison of daily $SW_{IN}$, $LW_{IN}$ and $LW_{OUT}$, as well as Rn and LE from the CoSEB-based datasets and mainstream products/datasets (including GLASS, BESS-Rad, BESSV2.0 and ETMonitor), with in situ observations at 44 test sites, respectively. Overall, the estimates from the CoSEB-based datasets

387 exhibited a closer agreement with in situ observations than those from mainstream

388 products/datasets, where the CoSEB-based datasets reduced the RMSE by 0.01 W/m$^2$

389 to 4.58 W/m$^2$ and increased the R² by 0.01 to 0.09 compared to mainstream products.

390 Specifically, the RMSE for the $SW_{IN}$, $LW_{IN}$, and $LW_{OUT}$ increased from 37.52 W/m$^2$,

391 22.47 W/m$^2$ and 13.78 W/m$^2$ in the CoSEB-based datasets to 37.53 W/m$^2$ ,23.37 W/m$^2$

392 and 16.46 W/m$^2$ in the GLASS, respectively, and for $SW_{IN}$ from 37.52 W/m$^2$ in the

393 CoSEB-based datasets to 40.87 W/m$^2$ in the BESS-Rad. Likewise, the RMSEs for daily

394 Rn and LE were 29.66 W/m$^2$ and 30.87 W/m$^2$ in the CoSEB-based datasets, which were

395 lower than those of 34.24 W/m$^2$ and 34.36 W/m$^2$ in BESSV2.0, respectively, as well as

396 those of 30.60 W/m$^2$ for Rn in GLASS and 33.62 W/m$^2$ for LE in ETMonitor.



398 **Fig. 6 Comparison of the daily downward shortwave radiation ($SW_{IN}$, the first column),**
399 **downward longwave radiation ($LW_{IN}$, the second column) and upward longwave radiation**
400 **($LW_{OUT}$, the third column) from the CoSEB-based datasets, GLASS and BESS-Rad with the**
401 **in situ observed $SW_{IN}$, $LW_{IN}$ and $LW_{OUT}$ at 44 test sites. The colorbar represents the normalized**
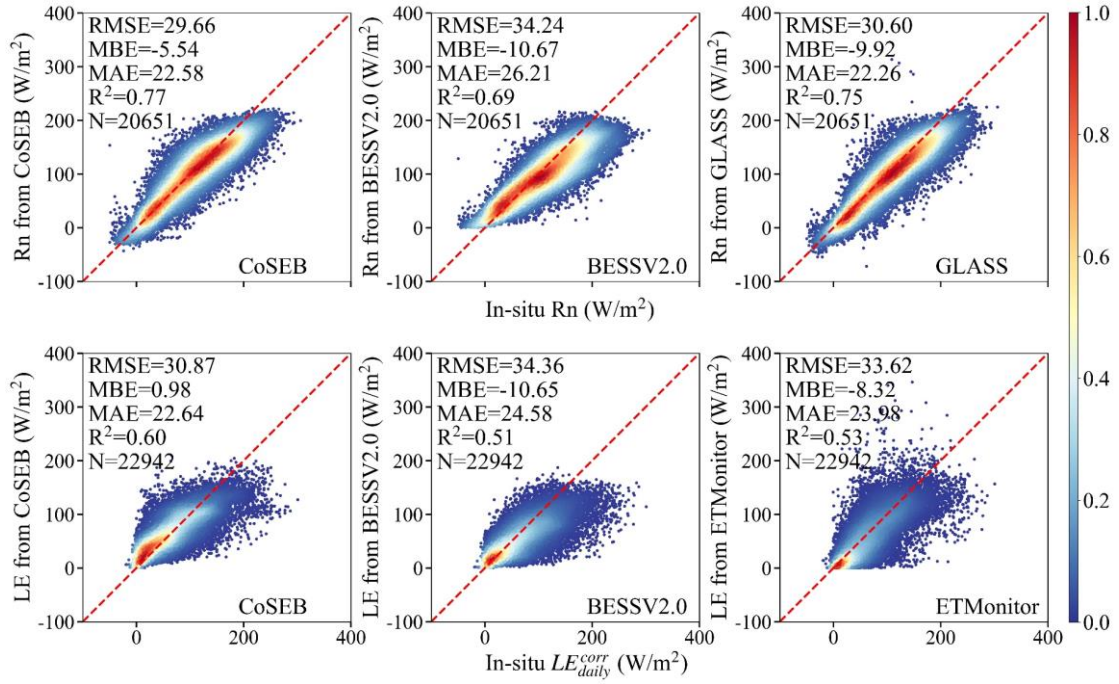402 **density of data points.**

403
404 **Fig. 7 Comparison of the daily net radiation (Rn, the upper row) and latent heat flux (LE, the**
405 **lower row) from the CoSEB-based datasets, BESSV2.0, GLASS and ETMonitor with the in**
406 **situ observed Rn, and energy imbalance-corrected LE ( $LE_{daily}^{corr}$ ) at 44 test sites. The colorbar**
407 **represents the normalized density of data points.**

408      Figs. 8, 9 and 10 compare the 8-day $SW_{IN}$, $LW_{IN}$ and $LW_{OUT}$, Rn and LE, as well as

409    H from the CoSEB-based datasets and mainstream products, with in situ observations

410    at 44 test sites, respectively. Overall, the CoSEB-based datasets outperformed the

411    mainstream products/datasets for all surface radiation and heat fluxes, where the

412    CoSEB-based datasets reduced the RMSE by 0.24 W/m² to 10.48 W/m² and increased

413    the R² by 0.01 to 0.38 compared to mainstream products. Specifically, for $SW_{IN}$, $LW_{IN}$

414    and $LW_{OUT}$, the RMSE increased from 18.54 W/m², 18.50 W/m² and 9.41 W/m² in the

415    CoSEB-based datasets to 21.35 W/m², 20.39 W/m² and 14.48 W/m² in the GLASS,

416    respectively, and for $SW_{IN}$ from 18.54 W/m² in the CoSEB-based datasets to 18.78

417    W/m² in the BESS-Rad. For Rn, the RMSE increased from 19.12 W/m² in the CoSEB-

418    based datasets to ~23 W/m² in the FLUXCOM and GLASS and to >27 W/m² in the

419    BESSV2.0, while the R² decreased from 0.82 in the CoSEB-based datasets to 0.75 in

420    the FLUXCOM and GLASS and to 0.62 in the BESSV2.0. Likewise, for LE, the RMSE

421    increased from 22.31 W/m² in the CoSEB-based datasets to ~25 W/m² in the

20

422 FLUXCOM, PML_V2, BESSV2.0 and ETMonitor, and to >32 W/m$^2$ in MOD16A2,

423 while the R$^2$ decreased from 0.67 in the CoSEB-based datasets to ~0.60 in the

424 FLUXCOM, PML_V2, BESSV2.0 and ETMonitor, and to <0.3 in the MOD16A1. For

425 H, the RMSE increased from 21.63 W/m$^2$ in the CoSEB-based datasets to 22.64 W/m$^2$

426 in the FLUXCOM.

427     The differences between the estimates from the CoSEB-based datasets and

428 mainstream datasets are likely multifactorial, arising from the simplification and

429 parameterization uncertainties in physics-based models, as well as the lack of physical

430 constraints, limited training samples, and incomplete consideration of influencing

431 factors in other machine-learning-based models.



432

433 **Fig. 8 Same as Fig. 6, but for the comparison at 8-day scale.**
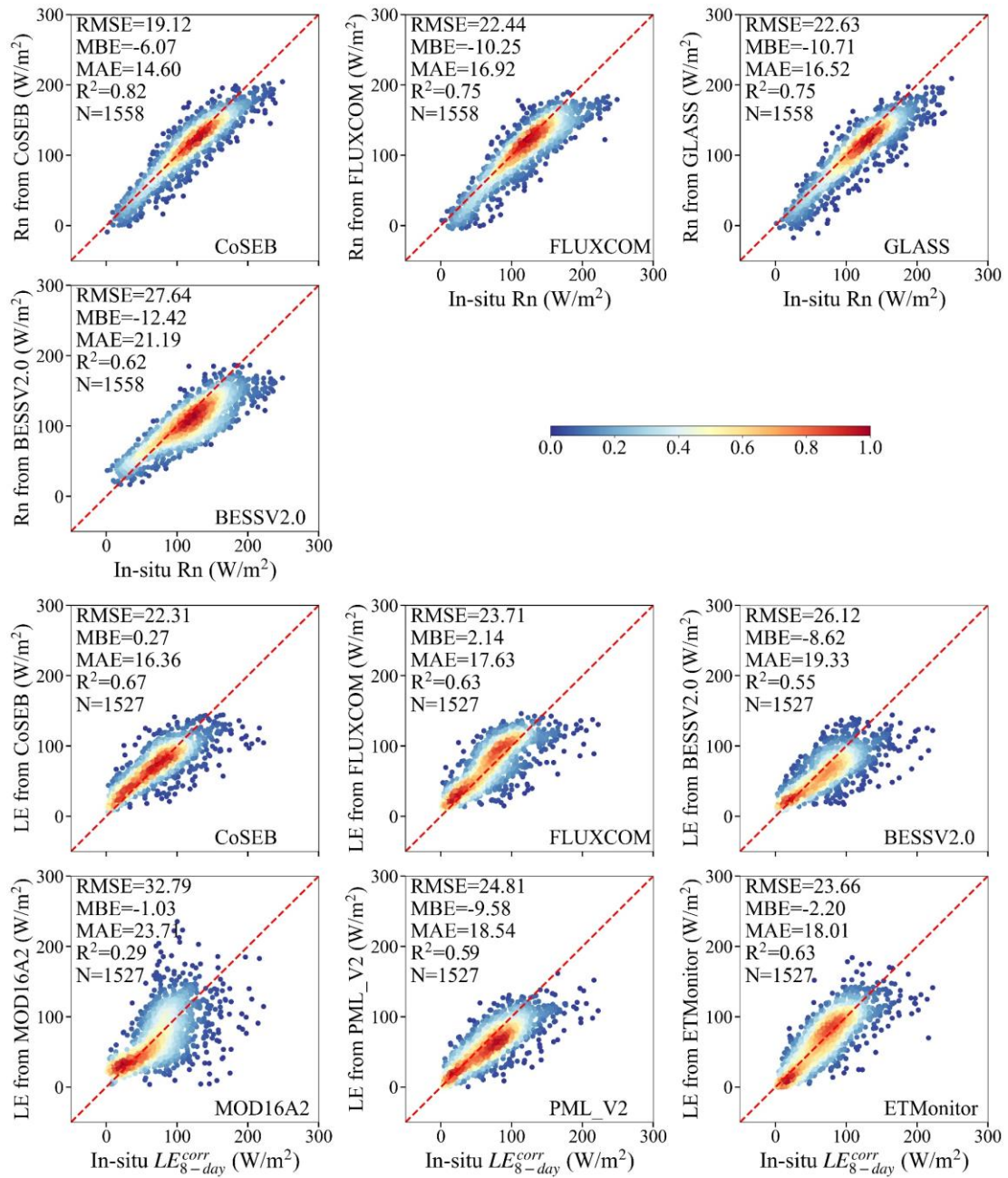
**Fig. 9 Comparison of the 8-day net radiation (Rn, the upper two rows) and latent heat flux (LE, the lower three rows) from the CoSEB-based datasets, FLUXCOM, BESSV2.0, GLASS, MOD16A2, PML_V2 and ETMonitor with in situ observed Rn, and energy imbalance-corrected LE ($LE_{8-day}^{corr}$) at 44 test sites. The colorbar represents the normalized density of data points.**
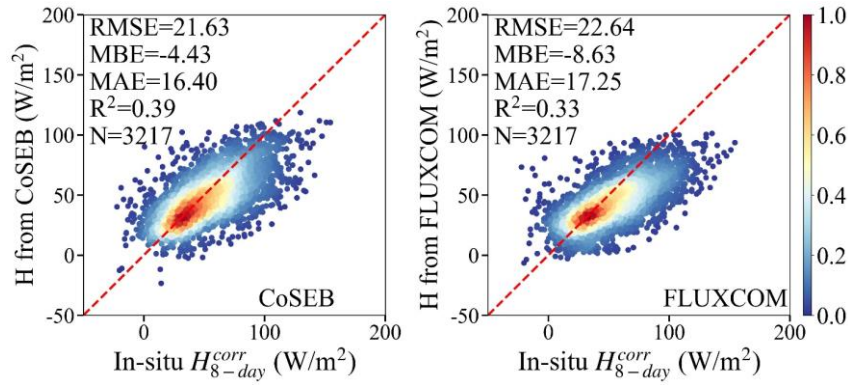
440

441 **Fig. 10 Comparison of the 8-day sensible heat flux (H) from the CoSEB-based datasets and**

442 **the FLUXCOM with the in situ energy imbalance-corrected H ($H_{8-day}^{corr}$) at 44 test sites. The**

443 **colorbar represents the normalized density of data points.**

444 **4.3 Spatial-temporal patterns of global land surface radiation and heat fluxes**

445      In addition to the validation and inter-comparison of the CoSEB-based datasets at

446 the site scale, we further inter-compared the estimates of land surface radiation and heat

447 fluxes from the CoSEB-based datasets and the mainstream products/datasets, in terms

448 of their global spatial and temporal patterns.

449      Figs. 11, 12 and 13 show the spatial distributions (excluding Greenland, Antarctic

450 continent, deserts, water bodies and permanent snow) and latitudinal profiles of the

451 global 0.05° mean annual $SW_{IN}$, $LW_{IN}$ and $LW_{OUT}$, Rn and LE, as well as H from 2001

452 to 2018, respectively, as derived from the CoSEB-based datasets and mainstream

453 products/datasets [i.e. GLASS, BESS-Rad, BESSV2.0, FLUXCOM, MOD16A2,

454 PML_V2 and ETMonitor, resampled to 0.05° using arithmetic averaging method or

455 cubic convolutional method if necessary]. Overall, the spatial patterns of the estimates

456 from the CoSEB-based datasets aligned well with those observed in these mainstream

457 products/datasets, though regional discrepancies were present. Specifically, the mean

458 annual $LW_{IN}$, $LW_{OUT}$, Rn, and LE generally exhibited decreasing trends from the equator

459 towards higher latitudes, peaking in regions such as the Amazon Rainforest, Congo

460 Rainforest, and the Malay Archipelago. In contrast, the higher mean annual $SW_{IN}$ and

461 H were mainly found in the Tibetan Plateau, southwestern U.S., mid-west Australia,

462 Sahel and Southern Africa, while the lower values were found in high-latitude regions

463    of >50°N. In the region with high values, the mean annual estimates of $SW_{IN}$ from the

464    CoSEB-based datasets were higher than those from GLASS but lower than those from

465    BESS-Rad, the estimates of $LW_{IN}$ and $LW_{OUT}$ from the CoSEB-based datasets were both

466    higher than those from GLASS, the estimates of Rn from the CoSEB-based datasets

467    were significantly higher than those from BESSV2.0, and comparable to or slightly

468    higher than those from FLUXCOM and GLASS, the estimates of LE from the CoSEB-

469    based datasets were close to those from BESSV2.0 and PML_V2, but slightly lower

470    than those from FLUXCOM, MOD16A2 and ETMonitor. Besides, the estimates of H

471    from the CoSEB-based datasets were higher than those from FLUXCOM in regions

472    with high values, while lower than those from FLUXCOM in regions with low values.
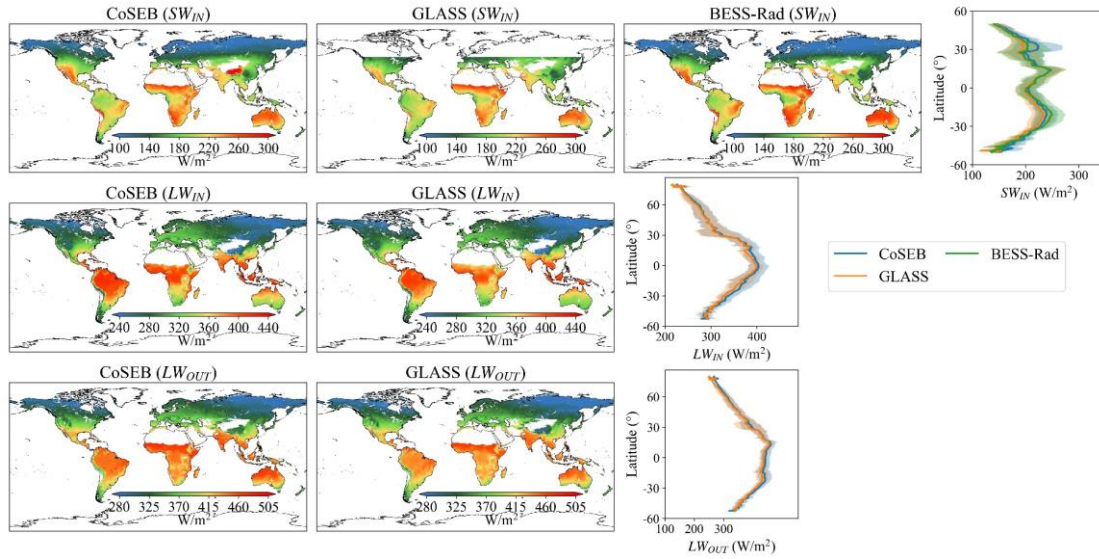
473

**Fig.11 Spatial patterns of global mean annual downward shortwave radiation ($SW_{IN}$, the first row), downward longwave radiation ($LW_{IN}$, the second row) and upward longwave radiation ($LW_{OUT}$, the third row) from 2001 to 2018 by CoSEB-based datasets, GLASS and BESS-Rad. The rightmost subfigure of each row represents the latitudinal profiles of mean annual $SW_{IN}$, $LW_{IN}$ and $LW_{OUT}$ from CoSEB-based datasets, GLASS and BESS-Rad, where the shaded area represents the variation of standard deviation for each product.**
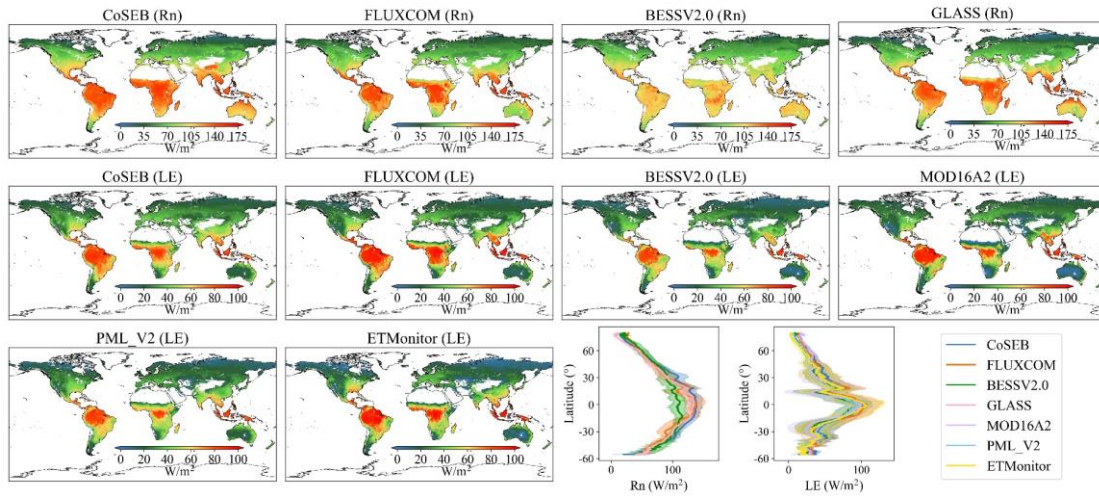


480

**Fig.12 Spatial patterns of global mean annual net radiation ($Rn$, the first row) and latent heat flux ($LE$, the second and third rows) from 2001 to 2018 by CoSEB-based datasets, FLUXCOM, BESSV2.0, MOD16A2, PML_V2, ETMonitor and GLASS. The last two subfigures of the third row represent the latitudinal profiles of mean annual Rn and LE from CoSEB-based datasets and these mainstream products/datasets, where the shaded area represents the variation of standard deviation for each product.**
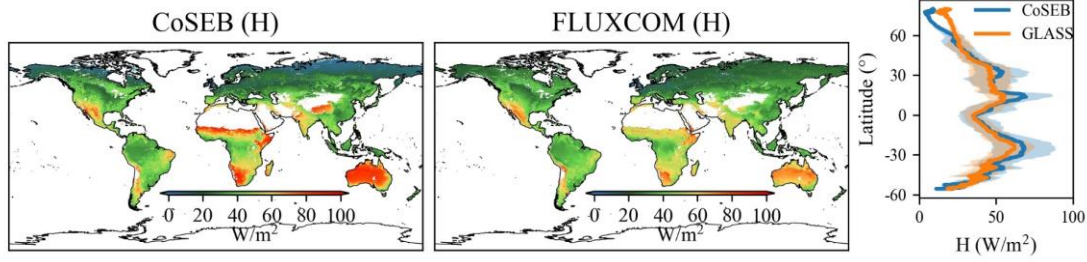
**Fig.13 Spatial patterns of global mean annual sensible heat flux (*H*) from 2001 to 2018 by CoSEB-based datasets and FLUXCOM. The rightmost subfigure represents the latitudinal profiles of mean annual H from CoSEB-based datasets and FLUXCOM, where the shaded area represents the variation of standard deviation for each product.**

The temporal evolutions of the global (excluding Greenland, Antarctic continent, deserts, water bodies and permanent snow) land surface radiation and heat fluxes derived from the CoSEB-based datasets and mainstream products/datasets from 2001 to 2018 were also investigated, as shown in Fig. 14. The results indicated that the temporal variation of each flux from the CoSEB-based datasets generally agreed well with those from mainstream products/datasets. The global annual mean estimates using area weighting average by the CoSEB-based datasets from 2001 to 2018 varied between ~185.22 and ~189.50 W/m² with the mean of ~187.23 W/m² for $SW_{IN}$, between ~32.67 and ~33.20 W/m² with the mean of ~32.96 W/m² for $SW_{OUT}$, between ~330.24 and ~334.14 W/m² with the mean of ~331.50 W/m² for $LW_{IN}$, between ~387.25 and ~390.82 W/m² with the mean of ~388.81 W/m² for $LW_{OUT}$, between ~95.41 and ~99.39 W/m² with the mean of 97.11 W/m² for Rn, between ~53.24 and ~56.37 W/m² with the mean of ~54.53 W/m² for LE, between ~40.44 and ~41.96 W/m² with the mean of ~41.29 W/m² for H, and between ~1.22 and ~1.52 W/m² with the mean of ~1.33 W/m² for G. For each radiation or heat flux, the annual mean estimates from the CoSEB-based datasets were overall higher than those from the mainstream products/datasets. In particular, the annual mean Rn estimates from the CoSEB-based datasets were higher than those from FLUXCOM, GLASS and BESSV2.0 sequentially, and the annual mean LE estimates from the CoSEB-based datasets were marginally higher than those from FLUXCOM, but substantially exceeded those from ETMonitor, PML_V2, MOD16A2 and BESSV2.0 sequentially. The anomaly-based analyses (Fig. S4 in the

513     Supplementary Material) reveal clear and coherent temporal trends of these radiation

514     and heat fluxes, which respond well to global climate change, such as increasing

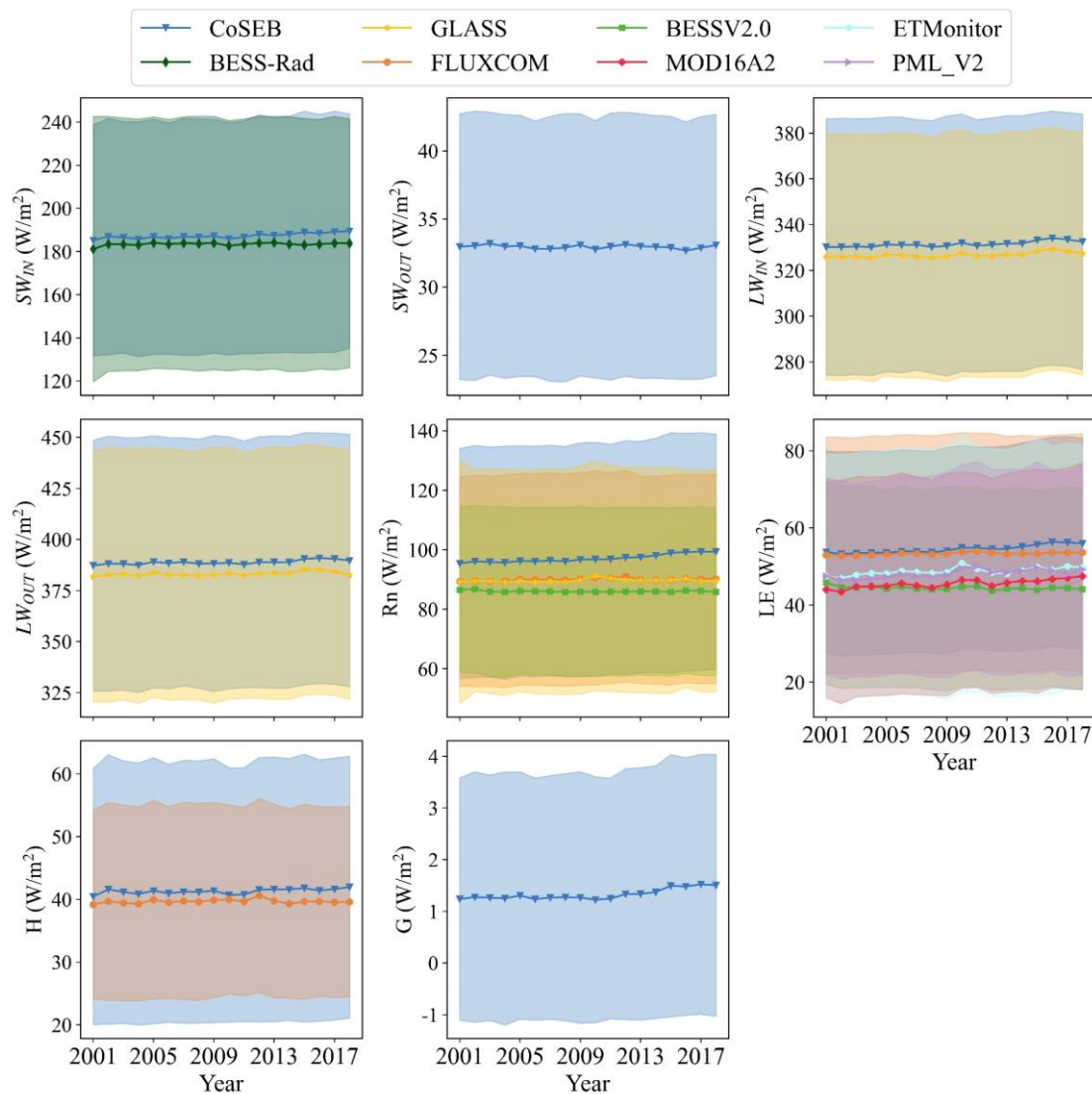515     atmospheric $CO_2$ and rising air temperatures.



516

517 **Fig. 14 Temporal variation of annual mean downward shortwave radiation ($SW_{IN}$), upward**

518 **shortwave radiation ($SW_{OUT}$), downward longwave radiation ($LW_{IN}$), upward longwave**

519 **radiation ($LW_{OUT}$), net radiation (Rn), latent heat flux (LE), sensible heat flux (H) and soil heat**

520 **flux (G) from 2001 to 2018 from the CoSEB-based datasets, BESS-Rad, GLASS, FLUXCOM,**

521 **BESSV2.0, PML_V2, MOD16A2 and ETMonitor. The shaded area represents the variation of**
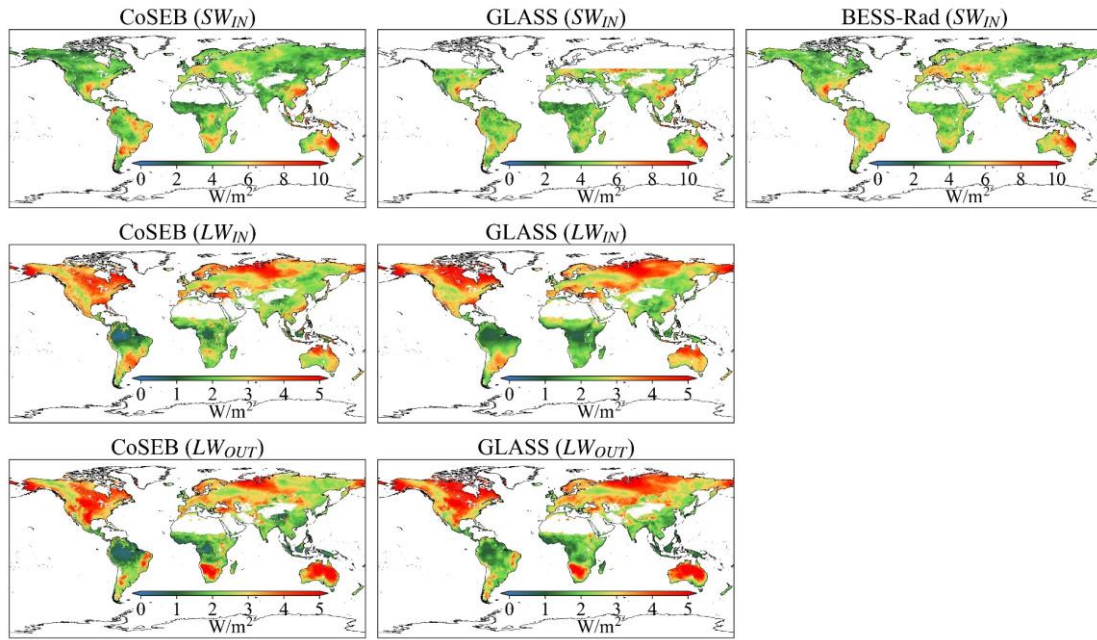
522 **the standard deviation for each product.**

**Fig. 15 Spatial distribution of interannual variability (standard deviation) of downward shortwave radiation *(SW_IN*, the first row), downward longwave radiation (*LW_IN*, the second row) and upward longwave radiation (*LW_OUT*, the third row) from 2001 to 2018 by the CoSEB-based datasets, GLASS and BESS-Rad.**

Figs. 15, 16 and 17 show the spatial patterns (excluding Greenland, Antarctic continent, deserts, water bodies and permanent snow) of interannual variability of $SW_{IN}$, $LW_{IN}$ and $LW_{OUT}$, Rn and LE, as well as H from 2001 to 2018, respectively, derived from the CoSEB-based datasets and mainstream products/datasets. In general, the estimates from the CoSEB-based datasets displayed similar interannual variability in space with those from the mainstream products/datasets. Specially, the estimates of $SW_{IN}$ from the CoSEB-based datasets, BESS-Rad, and GLASS exhibited a significant interannual variability mainly in northeastern Australia, eastern South America, Southeast China, and Southwest North America. The interannual variability of $LW_{IN}$ and $LW_{OUT}$ by the CoSEB-based datasets and GLASS displayed high values primarily at middle-to-high latitudes of the Northern Hemisphere and parts of Africa and Australia. The interannual variability of Rn observed by the CoSEB-based datasets was generally lower than that of GLASS, but higher than that of BESSV2.0 and FLUXCOM. The CoSEB-based datasets missed the strong interannual variability of LE as observed in MOD16A2, PML_V2 and ETMonitor in parts of Africa, Australia and eastern South

28

543 America. Furthermore, FLUXCOM exhibited the weakest interannual variability of LE

544 in almost all regions. The interannual variability of H derived from the CoSEB-based

545 datasets was higher than that from FLUXCOM, with stronger interannual variabilities

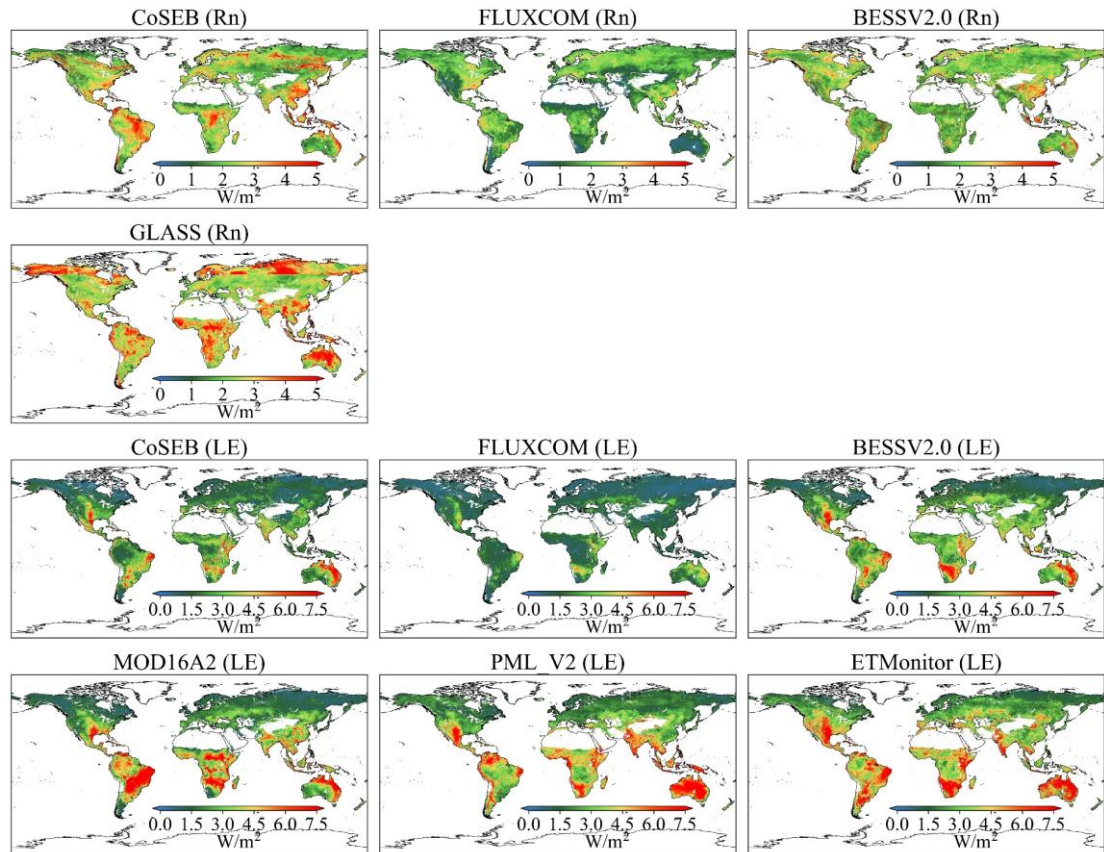546 mainly observed in parts of eastern South America, southern Africa, and northeastern

547 Australia.



548
549 **Fig. 16 Spatial distribution of interannual variability (standard deviation) of net radiation (Rn,**
550 **the first and second rows) and latent heat flux (LE, the third and fourth rows) from 2001 to**
551 **2018 by the CoSEB-based datasets, FLUXCOM, BESSV2.0, MOD16A2, PML_V2,**
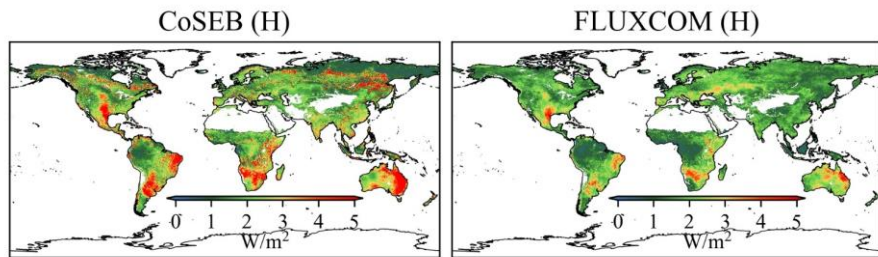552 **ETMonitor and GLASS.**



553
554 **Fig. 17 Spatial distribution of interannual variability (standard deviation) of sensible heat flux**
555 **(H) from 2001 to 2018 by the CoSEB-based datasets and FLUXCOM.**

**5 Discussion**

Accurately monitoring the spatial and temporal variations of global land surface radiation and heat fluxes is crucial for quantifying the exchange of radiation, heat and water between the land and atmosphere under global climate change (Chen et al., 2020; Du et al., 2024; Kim et al., 2023; Liang et al., 2006; Wang et al., 2020). However, although numerous global RS-based products/datasets of land surface radiation and heat fluxes have been developed using physical and/or statistical methods, they typically provide either merely a single flux or multiple fluxes (see Table 1) that are estimated separately from uncoordinated models (Huang et al., 2024; Jung et al., 2019; Sun et al., 2023; Tang et al., 2019), leading to noticeable radiation imbalance and/or heat imbalance when these products are combined for practical applications. To address these limitations, we generated high-accuracy global datasets of land surface radiation and heat fluxes from 2000 to 2020 that adhere to both radiation and heat conservation laws, using our proposed CoSEB model (Wang et al., 2025).

Our CoSEB model, integrating underlying physical principles of training datasets into machine learning technique to effectively learn the interrelations among multiple targeted outputs, was originally designed for coordinating estimates of global land surface energy balance components (Rn, LE, H and G) to satisfy the energy conservation (Wang et al., 2025). Inspired by the idea of constructing the original CoSEB model, we further incorporated land surface radiation fluxes into our model to simultaneously consider the physical constraints of both surface radiation and heat conservation principles, by renewing the CoSEB using multiple remote sensing and reanalysis datasets, as well as in-situ observations of $SW_{IN}$, $SW_{OUT}$, $LW_{IN}$, $LW_{OUT}$, Rn, LE, H and G. In selecting the 19 input variables to accommodate the additional target variables, prior knowledge derived from previous studies was employed to identify factors that exert significant influence on surface radiation and heat flux while maintaining relative inter-independence as much as possible (Jung et al., 2019; Mohan et al., 2020; Wang et al., 2021; Xian et al., 2024). This practice is commonly adopted

584 in data-driven models for estimating land surface water, energy, and carbon fluxes (Bai

585 et al., 2024; Elghawi et al., 2023; Han et al., 2023; O. & Orth, 2021). The importance

586 scores of the 19 different feature variables are exhibited in Table S4 in the

587 Supplementary Material, and downward solar radiation, the primary source of the

588 energy at the earth surface, is the most important input variable, consistent with the

589 results from our previous study (Wang et al., 2025). Although some of the selected

590 variables may exhibit a certain degree of multi-collinearity, each contributes unique and

591 physically meaningful information, supporting the inclusion of all variables in model

592 construction. Note that the variable importance, derived from the built-in method of the

593 random forests and potentially affected by multicollinearity among the input variables,

594 is presented only as a reference. Retaining all 19 feature variables ensures the model's

595 flexibility and generalization capability, enabling future incorporation of additional

596 representative ground-based observations for further training and improvement.

597 Besides, to investigate the impact of lagged effects of input variables on model

598 performance, experiments were also conducted by adding lagged variables (e.g., the air

599 temperature of the previous day) to the 19 input features. The results (Fig. S5 in the

600 Supplementary Material) showed almost no improvement in model accuracy,

601 suggesting that lagged effects on model performance were negligible within the CoSEB

602 framework for estimates of daily surface radiation and heat fluxes. Furthermore, to

603 better illustrate the effect of including additional radiation components ($SW_{IN}$, $SW_{OUT}$,

604 $LW_{IN}$ and $LW_{OUT}$) in the renewed CoSEB model compared with the original version by

605 Wang et al. (2025), we have tested the performance of a reconstructed model that

606 estimated only Rn, LE, H and G using the same independent variables and samples as

607 those in the renewed CoSEB model. The results (Fig. S6 in the supplementary material)

608 showed no significant differences in accuracy compared with those of the renewed

609 CoSEB model, indicating the expansion of radiation components did not compromise

610 model performance.

611    The main advantages of our CoSEB-based datasets of land surface radiation and

612    heat fluxes lie in that [1] they are the first data-driven global datasets that satisfy both

613    surface radiation balance ($SW_{IN}$ - $SW_{OUT}$ + $LW_{IN}$ - $LW_{OUT}$ = Rn) and heat balance (LE +

614    H + G = Rn) among the eight fluxes, as demonstrated by both the RIR and EIR of 0, [2]

615    the radiation and heat fluxes are characterized by high accuracies when validated

616    against in-situ measurements at 44 independent test sites (see the second paragraph in

617    Section 2.1), where (1) the RMSEs for daily estimates of $SW_{IN}$, $SW_{OUT}$, $LW_{IN}$, $LW_{OUT}$,

618    Rn, LE, H and G from the CoSEB-based datasets were 37.52 W/m$^2$, 14.20 W/m$^2$, 22.47

619    W/m$^2$, 13.78 W/m$^2$, 29.66 W/m$^2$, 30.87 W/m$^2$, 29.75 W/m$^2$ and 5.69 W/m$^2$, respectively,

620    as well as for 8-day estimates were 18.54 W/m$^2$, 12.19 W/m$^2$, 18.50 W/m$^2$, 9.41 W/m$^2$,

621    19.12 W/m$^2$, 22.31 W/m$^2$, 21.63 W/m$^2$ and 4.60 W/m$^2$, respectively, (2) the CoSEB-

622    based datasets, in comparison to the mainstream RS-based products/datasets (i.e.

623    GLASS, BESS-Rad, FLUXCOM, BESSV2.0, MOD16A2, PML_V2 and ETMonitor),

624    better agreed with the in situ observations at the 44 test sites, showing the RMSE

625    reductions ranging from 0.01 W/m$^2$ to 4.58 W/m$^2$ for $SW_{IN}$, $LW_{IN}$, $LW_{OUT}$, Rn and LE

626    at daily scale, and 0.24 W/m$^2$ to 10.48 W/m$^2$ for $SW_{IN}$, $LW_{IN}$, $LW_{OUT}$, Rn, LE and H at

627    8-day scale. Furthermore, the CoSEB-based datasets outperformed the ERA5-Land

628    reanalysis datasets in estimating surface energy fluxes (where $SW_{OUT}$, $LW_{OUT}$, Rn and

629    G for the ERA5-Land were inferred from surface radiation balance and heat balance),

630    particularly for $SW_{OUT}$, H and G, with RMSE reductions of 0.13-8.15 W/m$^2$ when

631    validated against in situ observations at the 44 test sites (Figs. S7 and S8 in the

632    Supplementary Material). Preliminary analysis indicates that the CoSEB-based datasets

633    exhibit spatial patterns consistent with those of mainstream RS-based datasets and Earth

634    system model outputs (see Fig. S9 in the supplementary material), suggesting that the

635    CoSEB-based datasets (or CoSEB framework) more broadly, are capable of

636    reproducing the large-scale spatial features of Earth system models. This capability

637    would be a great benefit to the community given the limitations associated with the high

638    computational cost and long execution time of Earth system models. More detailed

639    analysis about their similarities and differences can be further conducted in future work.

640  Our developed datasets could be potentially applied in many fields, including but

641 not limited to (1) exploring the spatial-temporal patterns of global land surface radiation

642 and heat flux (es) and their driving mechanisms over the past decades under global

643 change (e.g., rising $CO_2$ concentration, greening land surface and increasing air

644 temperature), (2) investigating the variability of land surface radiation and heat fluxes

645 caused by extreme events and human activities, e.g. afforestation or deforestation,

646 wildfire, air pollution, weather extremes and urbanization, (3) assessing the resources

647 of solar energy, geothermal energy, surface and ground water at regional and global

648 scales, (4) monitoring natural hazards, e.g. drought in agriculture and forestry.

649  The uncertainties of our datasets are relevant to (1) the data preprocessing, and (2)

650 the application of the CoSEB model across different spatial scales. Specifically, daily

651 averages of surface radiation and heat fluxes for each day were obtained for analysis

652 from good-quality half-hourly observations when the fraction of these good-quality

653 half-hourly observations was greater than 80% in a day, due to the lack of consensus on

654 the method for aggregating gapped half-hourly observations to daily data (Tang et al.,

655 2024a; Yao et al., 2017; Zheng et al., 2022). Simple temporal interpolation of half-

656 hourly in situ observations, which could therefore introduce substantial uncertainties,

657 was not applied, because surface radiation and heat fluxes are sensitive to short-term

658 variations in meteorological conditions and their intraday dynamics are often complex.

659 Likewise, since there was no agreement on how to correct for the energy imbalance of

660 turbulent heat fluxes, we adopted the most widely applied Bowen ratio method to

661 enforce energy closure between $Rn - G$ and $LE + H$ (Castelli et al., 2018; Twine et

662 al., 2000; Zhang et al., 2021). Another potential source of uncertainty arises from

663 differences in meteorological reanalysis data caused by spatial downscaling, which, as

664 demonstrated in our previous study (Wang et al., 2025, the last paragraph of Section

665 5.1), has a relatively small impact on model estimates by the machine-learning-based

666 CoSEB model combined with finer-resolution surface-related variables that partially

667 compensate for the spatial heterogeneity and localized variations not captured by the

668    coarse-resolution datasets. These data preprocessing had an effect on the construction

669    of the renewed CoSEB model, which may further affect the global datasets. Moreover,

670    the renewed CoSEB model was constructed at the spatial scale of 500 m to match the

671    footprints of the in situ EC observations, but applied at the spatial resolution of 0.05°

672    to generate global datasets, mainly limited by the computing and storage capabilities of

673    our personal computers. However, the CoSEB-based datasets have also been validated

674    and inter-compared at 44 independent test sites to demonstrate that the difference in

675    spatial scale would not much affect the performance of the datasets. Note that the 302

676    sites used for training, validation, and testing are predominantly located in the Northern

677    Hemisphere, reflecting the inherent uneven distribution of the global flux networks.

678    Although these sites cover a wide range of land cover types and climate regimes,

679    thereby providing substantial heterogeneity for model development, the limited

680    representation of the Southern Hemisphere may introduce uncertainties in the

681    estimation of surface radiation and heat fluxes for certain ecosystems and soil types. In

682    the future, enhancing the flux observation network coverage in the Southern

683    Hemisphere, particularly in South America and Africa, and incorporating these

684    observations into the CoSEB framework would help further improve the accuracy of

685    surface radiation and heat flux estimates in these regions. Furthermore, the radiation

686    and heat balance in this study refers specifically to the conservation among the eight

687    variables (i.e., $SW_{IN}$, $LW_{IN}$, $SW_{OUT}$, $LW_{OUT}$, Rn, LE, G, H), which constitute the major

688    components of the surface energy budget, and does not account for energy introduced

689    by disturbance-related processes such as wildfires and volcanic eruptions. Despite these

690    uncertainties, it is worth emphasizing that our work was the first attempt to innovatively

691    develop data-driven energy-conservation datasets of global land surface radiation and

692    heat fluxes with high accuracies.


693    **6 Data availability**

694        The energy-conservation datasets of global land surface radiation and heat fluxes

695    generated by the CoSEB model with spatial-temporal resolutions of daily and 0.05°

696     from Feb.26, 2000 to Dec.31, 2020 are freely available through the National Tibetan

697     Plateau Data Center at https://doi.org/10.11888/Terre.tpdc.302559 (Tang et al., 2025a)

698     and     through     the     Science     Data     Bank     (ScienceDB)     at

699     https://doi.org/10.57760/sciencedb.27228 (Tang et al., 2025b).

700     **7 Summary and Conclusion**

701         This study for the first time developed data-driven energy-conservation datasets

702     of global land surface radiation and heat fluxes using our CoSEB model renewed based

703     on GLASS and MODIS products, ERA5-Land reanalysis datasets, topographic data,

704     $CO_2$ concentration data, and observations at 258 EC sites worldwide.

705         The CoSEB-based datasets of land surface radiation and heat fluxes are the first

706     data-driven global datasets that satisfy both surface radiation balance ($SW_{IN}$ - $SW_{OUT}$ +

707     $LW_{IN}$ - $LW_{OUT}$ = Rn) and heat balance (LE + H + G = Rn) among the eight fluxes.

708     Meanwhile, the CoSEB-based datasets outperformed the mainstream products/datasets

709     in accuracy. Specifically, at 44 independent test sites, the RMSEs ($R^2$) for daily

710     estimates of $SW_{IN}$, $SW_{OUT}$, $LW_{IN}$, $LW_{OUT}$, Rn, LE, H and G from the CoSEB-based

711     datasets were 37.52 W/m$^2$ (0.81), 14.20 W/m$^2$ (0.42), 22.47 W/m$^2$ (0.90), 13.78 W/m$^2$

712     (0.95), 29.66 W/m$^2$ (0.77), 30.87 W/m$^2$ (0.60), 29.75 W/m$^2$ (0.44) and 5.69 W/m$^2$ (0.44),

713     respectively, as well as for 8-day estimates were 18.54 W/m$^2$ (0.87), 12.19 W/m$^2$ (0.39),

714     18.50 W/m$^2$ (0.92), 9.41 W/m$^2$ (0.97), 19.12 W/m$^2$ (0.82), 22.31 W/m$^2$ (0.67), 21.63

715     W/m$^2$ (0.39) and 4.60 W/m$^2$ (0.47), respectively. Moreover, the estimates from the

716     CoSEB-based datasets in comparison to those from the mainstream products/datasets

717     reduced the RMSE by 0.01 W/m$^2$ to 4.58 W/m$^2$ and increased the $R^2$ by 0.01 to 0.09

718     for $SW_{IN}$, $LW_{IN}$, $LW_{OUT}$, Rn and LE at daily scale, and reduced the RMSE by 0.24 W/m$^2$

719     to 10.48 W/m$^2$ and increased the $R^2$ by 0.01 to 0.38 for $SW_{IN}$, $LW_{IN}$, $LW_{OUT}$, Rn, LE and

720     H at 8-day scale, when these estimates were validated against in situ observations at 44

721     independent test sites. Furthermore, the CoSEB-based datasets effectively captured the

722     spatial-temporal variability of global land surface radiation and heat fluxes, aligning

723     well with those from the mainstream products.

724    Our developed datasets hold significant potential for application across diverse

725    fields such as agriculture, forestry, hydrology, meteorology, ecology, and environmental

726    science. They can facilitate comprehensive studies on the variability, impacts, responses,

727    adaptation strategies, and mitigation measures of global and regional land surface

728    radiation and heat fluxes under the influences of climate change and human activities.

729    These datasets will provide valuable insights and data support for scientific research,

730    policy-making, and environmental management, advancing global solutions to address

731    climate change.


732    **Author contribution**

733    JW: Writing – original draft, Visualization, Software, Formal analysis, Data

734    curation. RT: Writing – original draft, Validation, Supervision, Methodology, Funding

735    acquisition, Formal analysis, Conceptualization. ML: Writing – review & editing,

736    Validation. ZL: Writing – review & editing.


737    **Competing interests**

738    The authors declare that they have no conflict of interest.

747    **References**

748    Bai, Y., Mallick, K., Hu, T., Zhang, S., Yang, S. and Ahmadi, A.: Integrating machine
749        learning with thermal-driven analytical energy balance model improved

750    terrestrial evapotranspiration estimation through enhanced surface conductance,
751    Remote Sens. Environ., 311, 114308. 10.1016/j.rse.2024.114308, 2024.

752 Bartkowiak, P., Ventura, B., Jacob, A. and Castelli, M.: A Copernicus-based
753    evapotranspiration dataset at 100 m spatial resolution over four Mediterranean
754    basins, Earth Syst. Sci. Data, 16, 4709-4734. 10.5194/essd-16-4709-2024, 2024.

755 Berbery, E. H., Mitchell, K. E., Benjamin, S., Smirnova, T., Ritchie, H., Hogue, R. and
756    Radeva, E.: Assessment of land‐surface energy budgets from regional and
757    global models, J. Geophys. Res.-Atmos., 104, 19329-19348.
758    10.1029/1999jd900128, 1999.

759 Betts, A. K., Ball, J. H., Beljaars, A. C. M., Miller, M. J. and Viterbo, P. A.: The land
760    surface‐atmosphere interaction: A review based on observational and global
761    modeling perspectives, J. Geophys. Res.-Atmos., 101, 7209-7225.
762    10.1029/95jd02135, 1996.

763 Castelli, M., Anderson, M. C., Yang, Y., Wohlfahrt, G., Bertoldi, G., Niedrist, G.,
764    Hammerle, A., Zhao, P., Zebisch, M. and Notarnicola, C.: Two-source energy
765    balance modeling of evapotranspiration in Alpine grasslands, Remote Sens.
766    Environ., 209, 327-342. 10.1016/j.rse.2018.02.062, 2018.

767 Chen, J., He, T., Jiang, B. and Liang, S.: Estimation of all-sky all-wave daily net
768    radiation at high latitudes from MODIS data, Remote Sens. Environ., 245,
769    111842. 10.1016/j.rse.2020.111842, 2020.

770 de Wit, A. J. W., Boogaard, H. L. and van Diepen, C. A.: Spatial resolution of
771    precipitation and radiation: The effect on regional crop yield forecasts, Agric.
772    For. Meteorol., 135, 156-168. 10.1016/j.agrformet.2005.11.012, 2005.

773 Du, Y., Wang, T., Zhou, Y., Letu, H., Li, D. and Xian, Y.: Towards user-friendly all-sky
774    surface longwave downward radiation from space: General scheme and product,
775    Bull. Amer. Meteorol. Soc., 105, E1303–E1319. 10.1175/bams-d-23-0126.1,
776    2024.

777 ElGhawi, R., Kraft, B., Reimers, C., Reichstein, M., Körner, M., Gentine, P. and
778    Winkler, A. J.: Hybrid modeling of evapotranspiration: inferring stomatal and
779    aerodynamic resistances using combined physics-based and machine learning,
780    Environ. Res. Lett., 18, 034039. 10.1088/1748-9326/acbbe0, 2023.

781 Ersi, C., Sudu, B., Song, Z., Bao, Y., Wei, S., Zhang, J., Tong, Z., Liu, X., Le, W. and
782    Rina, S.: The potential of NIRvP in estimating evapotranspiration, Remote Sens.
783    Environ., 315, 114405. 10.1016/j.rse.2024.114405, 2024.

784 Han, Q., Zeng, Y., Zhang, L., Wang, C., Prikaziuk, E., Niu, Z. and Su, B.: Global long
785    term daily 1 km surface soil moisture dataset with physics informed machine
786    learning, Sci. Data, 10, 101. 10.1038/s41597-023-02011-7, 2023.

787 Huang, J., Yu, H., Guan, X., Wang, G. and Guo, R.: Accelerated dryland expansion
788    under climate change, Nat. Clim. Chang., 6, 166-171. 10.1038/nclimate2837,
789    2015.

790 Huang, L., Luo, Y., Chen, J. M., Tang, Q., Steenhuis, T., Cheng, W. and Shi, W.:
791    Satellite-based near-real-time global daily terrestrial evapotranspiration

792    estimates, Earth Syst. Sci. Data, 16, 3993-4019. 10.5194/essd-16-3993-2024,
793    2024.

794 Jia, B., Xie, Z., Dai, A., Shi, C. and Chen, F.: Evaluation of satellite and reanalysis
795    products of downward surface solar radiation over East Asia: Spatial and
796    seasonal variations, J. Geophys. Res.-Atmos., 118, 3431-3446.
797    10.1002/jgrd.50353, 2013.

798 Jiang, B., Zhang, Y., Liang, S., Wohlfahrt, G., Arain, A., Cescatti, A., Georgiadis, T., Jia,
799    K., Kiely, G., Lund, M., Montagnani, L., Magliulo, V., Ortiz, P. S., Oechel, W.,
800    Vaccari, F. P., Yao, Y. and Zhang, X.: Empirical estimation of daytime net
801    radiation from shortwave radiation and ancillary information, Agric. For.
802    Meteorol., 211-212, 23-36. 10.1016/j.agrformet.2015.05.003, 2015.

803 Jiao, B., Su, Y., Li, Q., Manara, V. and Wild, M.: An integrated and homogenized global
804    surface solar radiation dataset and its reconstruction based on a convolutional
805    neural network approach, Earth Syst. Sci. Data, 15, 4519-4535. 10.5194/essd-
806    15-4519-2023, 2023.

807 Jung, M., Koirala, S., Weber, U., Ichii, K., Gans, F., Camps-Valls, G., Papale, D.,
808    Schwalm, C., Tramontana, G. and Reichstein, M.: The FLUXCOM ensemble of
809    global land-atmosphere energy fluxes, Sci. Data, 6, 74. 10.1038/s41597-019-
810    0076-8, 2019.

811 Kim, Y., Park, H., Kimball, J. S., Colliander, A. and McCabe, M. F.: Global estimates
812    of daily evapotranspiration using SMAP surface and root-zone soil moisture,
813    Remote Sens. Environ., 298, 113803. 10.1016/j.rse.2023.113803, 2023.

814 Li, B., Ryu, Y., Jiang, C., Dechant, B., Liu, J., Yan, Y. and Li, X.: BESSv2.0: A satellite-
815    based and coupled-process model for quantifying long-term global land–
816    atmosphere fluxes, Remote Sens. Environ., 295, 113696.
817    10.1016/j.rse.2023.113696, 2023.

818 Liang, S., Wang, D., He, T. and Yu, Y.: Remote sensing of earth's energy budget:
819    synthesis and review, Int. J. Digit. Earth, 12, 737-780.
820    10.1080/17538947.2019.1597189, 2019.

821 Liang, S., Zheng, T., Liu, R., Fang, H., Tsay, S. C. and Running, S.: Estimation of
822    incident photosynthetically active radiation from Moderate Resolution Imaging
823    Spectrometer data, J. Geophys. Res.-Atmos., 111, D15208.
824    10.1029/2005jd006730, 2006.

825 Liu, S., Xu, Z., Song, L., Zhao, Q., Ge, Y., Xu, T., Ma, Y., Zhu, Z., Jia, Z. and Zhang,
826    F.: Upscaling evapotranspiration measurements from multi-site to the satellite
827    pixel scale over heterogeneous land surfaces, Agric. For. Meteorol., 230, 97-113.
828    10.1016/j.agrformet.2016.04.008, 2016.

829 Mohan, M. M. P., Kanchirapuzha, R. and Varma, M. R. R.: Review of approaches for
830    the estimation of sensible heat flux in remote sensing-based evapotranspiration
831    models, J. Appl. Remote Sens., 14, 041501-041501. 10.1117/1.Jrs.14.041501,
832    2020.

833 Mu, Q., Zhao, M. and Running, S. W.: Improvements to a MODIS global terrestrial

834    evapotranspiration algorithm, Remote Sens. Environ., 115, 1781-1800.
835         10.1016/j.rse.2011.02.019, 2011.

836    Mueller, R. W., Matsoukas, C., Gratzki, A., Behr, H. D. and Hollmann, R.: The CM-
837         SAF operational scheme for the satellite based retrieval of solar surface
838         irradiance — A LUT based eigenvector hybrid approach, Remote Sens. Environ.,
839         113, 1012-1024. 10.1016/j.rse.2009.01.012, 2009.

840    Muñoz-Sabater, J., Dutra, E., Agustí-Panareda, A., Albergel, C., Arduini, G., Balsamo,
841         G., Boussetta, S., Choulga, M., Harrigan, S., Hersbach, H., Martens, B.,
842         Miralles, D. G., Piles, M., Rodríguez-Fernández, N. J., Zsoter, E., Buontempo,
843         C. and Thépaut, J.-N.: ERA5-Land: a state-of-the-art global reanalysis dataset
844         for land applications, Earth Syst. Sci. Data, 13, 4349-4383. 10.5194/essd-13-
845         4349-2021, 2021.

846    Nemani, R. R., Keeling, C. D., Hashimoto, H., Jolly, W. M., Piper, S. C., Tucker, C. J.,
847         Myneni, R. B. and Running, S. W.: Climate-driven increases in global terrestrial
848         net primary production from 1982 to 1999, Science, 300, 1560-1563.
849         10.1126/science.1082750, 2003.

850    O., S. and Orth, R.: Global soil moisture data derived through machine learning trained
851         with in-situ measurements, Sci. Data, 8, 170. 10.1038/s41597-021-00964-1,
852         2021.

853    Peng, Z., Letu, H., Wang, T., Shi, C., Zhao, C., Tana, G., Zhao, N., Dai, T., Tang, R.,
854         Shang, H., Shi, J. and Chen, L.: Estimation of shortwave solar radiation using
855         the artificial neural network from Himawari-8 satellite imagery over China,
856         Journal of Quantitative Spectroscopy and Radiative Transfer, 240, 106672.
857         10.1016/j.jqsrt.2019.106672, 2020.

858    Rios, G. and Ramamurthy, P.: A novel model to estimate sensible heat fluxes in urban
859         areas using satellite-derived data, Remote Sens. Environ., 270, 112880.
860         10.1016/j.rse.2021.112880, 2022.

861    Ryu, Y., Jiang, C., Kobayashi, H. and Detto, M.: MODIS-derived global land products
862         of shortwave radiation and diffuse and total photosynthetically active radiation
863         at 5 km resolution from 2000, Remote Sens. Environ., 204, 812-825.
864         10.1016/j.rse.2017.09.021, 2018.

865    Sellers, P. J., Dickinson, R. E., Randall, D. A., Betts, A. K., Hall, F. G., Berry, J. A.,
866         Collatz, G. J., Denning, A. S., Mooney, H. A., Nobre, C. A., Sato, N., Field, C.
867         B. and Henderson-Sellers, A.: Modeling the Exchanges of Energy, Water, and
868         Carbon Between Continents and the Atmosphere, Science, 275, 502-509.
869         10.1126/science.275.5299.502, 1997.

870    Sun, S., Bi, Z., Xiao, J., Liu, Y., Sun, G., Ju, W., Liu, C., Mu, M., Li, J., Zhou, Y., Li,
871         X., Liu, Y. and Chen, H.: A global 5 km monthly potential evapotranspiration
872         dataset (1982–2015) estimated by the Shuttleworth–Wallace model, Earth Syst.
873         Sci. Data, 15, 4849-4876. 10.5194/essd-15-4849-2023, 2023.

874    Tang, R., Peng, Z., Liu, M., Li, Z.-L., Jiang, Y., Hu, Y., Huang, L., Wang, Y., Wang, J.,
875         Jia, L., Zheng, C., Zhang, Y., Zhang, K., Yao, Y., Chen, X., Xiong, Y., Zeng, Z.

876      and Fisher, J. B.: Spatial-temporal patterns of land surface evapotranspiration
877      from global products, Remote Sens. Environ., 304, 114066.
878      10.1016/j.rse.2024.114066, 2024a.

879 Tang, R., Wang, J., Liu, M. and Li, Z.-L.: Energy-conservation datasets of global land
880      surface radiation and heat fluxes from 2000-2020 generated by CoSEB,
881      National Tibetan Plateau / Third Pole Environment Data Center. [data set],
882      https://doi.org/10.11888/Terre.tpdc.302559, 2025a.

883 Tang, R., Wang, J., Liu, M. and Li, Z.-L.: Energy-conservation datasets of global land
884      surface radiation and heat fluxes from 2000-2020 generated by CoSEB, Science
885      Data Bank: Science Data Bank. [data set],
886      https://doi.org/10.57760/sciencedb.27228, 2025b.

887 Tang, W., He, J., Qi, J. and Yang, K.: A dense station-based, long-term and high-
888      accuracy dataset of daily surface solar radiation in China, Earth Syst. Sci. Data,
889      15, 4537-4551. 10.5194/essd-15-4537-2023, 2023.

890 Tang, W., He, J., Shao, C., Song, J., Yuan, Z. and Yan, B.: Constructing a long-term
891      global dataset of direct and diffuse radiation (10 km, 3 h, 1983–2018) separating
892      from the satellite-based estimates of global radiation, Remote Sens. Environ.,
893      311, 114292. 10.1016/j.rse.2024.114292, 2024b.

894 Tang, W., Yang, K., Qin, J., Li, X. and Niu, X.: A 16-year dataset (2000–2015) of high-
895      resolution (3 h, 10 km) global surface solar radiation, Earth Syst. Sci. Data, 11,
896      1905-1915. 10.5194/essd-11-1905-2019, 2019.

897 Twine, T. E., Kustas, W. P., Norman, J. M., Cook, D. R., Houser, P. R., Meyers, T. P.,
898      Prueger, J. H., Starks, P. J. and Wesely, M. L.: Correcting eddy-covariance flux
899      underestimates over a grassland, Agric. For. Meteorol., 103, 279-300.
900      10.1016/S0168-1923(00)00123-4, 2000.

901 van der Tol, C.: Validation of remote sensing of bare soil ground heat flux, Remote Sens.
902      Environ., 121, 275-286. 10.1016/j.rse.2012.02.009, 2012.

903 Wang, D., Liang, S., He, T. and Shi, Q.: Estimation of Daily Surface Shortwave Net
904      Radiation From the Combined MODIS Data, IEEE Trans. Geosci. Remote
905      Sensing, 53, 5519-5529. 10.1109/tgrs.2015.2424716, 2015.

906 Wang, D., Liang, S., Li, R. and Jia, A.: A synergic study on estimating surface
907      downward shortwave radiation from satellite data, Remote Sens. Environ., 264,
908      112639. 10.1016/j.rse.2021.112639, 2021.

909 Wang, J., Tang, R., Liu, M., Jiang, Y., Huang, L. and Li, Z.-L.: Coordinated estimates
910      of 4-day 500 m global land surface energy balance components, Remote Sens.
911      Environ., 326, 114795. 10.1016/j.rse.2025.114795, 2025.

912 Wang, K. C., Dickinson, R. E., Wild, M. and Liang, S.: Atmospheric impacts on climatic
913      variability of surface incident solar radiation, Atmos. Chem. Phys., 12, 9581-
914      9592. 10.5194/acp-12-9581-2012, 2012.

915 Wang, T., Shi, J., Ma, Y., Letu, H. and Li, X.: All-sky longwave downward radiation
916      from satellite measurements: General parameterizations based on LST, column
917      water vapor and cloud top temperature, ISPRS-J. Photogramm. Remote Sens.,

161, 52-60. 10.1016/j.isprsjprs.2020.01.011, 2020.

Wang, Y., Hu, J., Li, R., Song, B. and Hailemariam, M.: Remote sensing of daily evapotranspiration and gross primary productivity of four forest ecosystems in East Asia using satellite multi-channel passive microwave measurements, Agric. For. Meteorol., 339, 109595. 10.1016/j.agrformet.2023.109595, 2023.

Wild, M.: Global dimming and brightening: A review, J. Geophys. Res.-Atmos., 114, D00D16. 10.1029/2008jd011470, 2009.

Wild, M., Folini, D., Schär, C., Loeb, N., Dutton, E. G. and König-Langlo, G.: The global energy balance from a surface perspective, Clim. Dyn., 40, 3107-3134. 10.1007/s00382-012-1569-8, 2012.

Wild, M. and Liepert, B.: The Earth radiation balance as driver of the global hydrological cycle, Environ. Res. Lett., 0, 025203. 10.1088/1748-9326/5/2/025003, 2010.

Xia, X. A., Wang, P. C., Chen, H. B. and Liang, F.: Analysis of downwelling surface solar radiation in China from National Centers for Environmental Prediction reanalysis, satellite estimates, and surface observations, J. Geophys. Res.-Atmos., 111, D09103. 10.1029/2005jd006405, 2006.

Xian, Y., Wang, T., Leng, W., Letu, H., Shi, J., Wang, G., Yan, X. and Yuan, H.: Can Topographic Effects on Solar Radiation Be Ignored: Evidence From the Tibetan Plateau, Geophys. Res. Lett., 51, e2024GL108653. 10.1029/2024gl108653, 2024.

Xu, J., Liang, S. and Jiang, B.: A global long-term (1981–2019) daily land surface radiation budget product from AVHRR satellite data using a residual convolutional neural network, Earth Syst. Sci. Data, 14, 2315-2341. 10.5194/essd-14-2315-2022, 2022a.

Xu, J., Liang, S., Ma, H. and He, T.: Generating 5 km resolution 1981–2018 daily global land surface longwave radiation products from AVHRR shortwave and longwave observations using densely connected convolutional neural networks, Remote Sens. Environ., 280, 113223. 10.1016/j.rse.2022.113223, 2022b.

Yao, Y., Liang, S., Li, X., Chen, J., Liu, S., Jia, K., Zhang, X., Xiao, Z., Fisher, J. B., Mu, Q., Pan, M., Liu, M., Cheng, J., Jiang, B., Xie, X., Grünwald, T., Bernhofer, C. and Roupsard, O.: Improving global terrestrial evapotranspiration estimation using support vector machine by integrating three process-based algorithms, Agric. For. Meteorol., 242, 55-74. 10.1016/j.agrformet.2017.04.011, 2017.

Yu, L., Qiu, G. Y., Yan, C., Zhao, W., Zou, Z., Ding, J., Qin, L. and Xiong, Y.: A global terrestrial evapotranspiration product based on the three-temperature model with fewer input parameters and no calibration requirement, Earth Syst. Sci. Data, 14, 3673-3693. 10.5194/essd-14-3673-2022, 2022.

Zhang, C., Long, D., Zhang, Y., Anderson, M. C., Kustas, W. P. and Yang, Y.: A decadal (2008–2017) daily evapotranspiration data set of 1 km spatial resolution and spatial completeness across the North China Plain using TSEB and data fusion, Remote Sens. Environ., 262, 112519. 10.1016/j.rse.2021.112519, 2021.

960 Zhang, J., Zhao, L., Deng, S., Xu, W. and Zhang, Y.: A critical review of the models
961     used to estimate solar radiation, Renew. Sust. Energ. Rev., 70, 314-329.
962     10.1016/j.rser.2016.11.124, 2017.

963 Zhang, K., Kimball, J. S., Nemani, R. R. and Running, S. W.: A continuous satellite‐
964     derived global record of land surface evapotranspiration from 1983 to 2006,
965     Water Resour. Res., 46, W09522. 10.1029/2009wr008800, 2010.

966 Zhang, X., Liang, S., Zhou, G., Wu, H. and Zhao, X.: Generating Global LAnd Surface
967     Satellite incident shortwave radiation and photosynthetically active radiation
968     products from multiple satellite data, Remote Sens. Environ., 152, 318-332.
969     10.1016/j.rse.2014.07.003, 2014.

970 Zhang, Y., Kong, D., Gan, R., Chiew, F. H. S., McVicar, T. R., Zhang, Q. and Yang, Y.:
971     Coupled estimation of 500 m and 8-day resolution global evapotranspiration
972     and gross primary production in 2002–2017, Remote Sens. Environ., 222, 165-
973     182. 10.1016/j.rse.2018.12.031, 2019.

974 Zheng, C., Jia, L. and Hu, G.: Global land surface evapotranspiration monitoring by
975     ETMonitor model driven by multi-source satellite earth observations, J. Hydrol.,
976     613, 128444. 10.1016/j.jhydrol.2022.128444, 2022.

977